Scanning Microscopy

Volume 1995
Number 9 *Luminescence*

Article 11

1995

Optical Studies of InGaAs/GaAs Multiple Quantum Wells (MQW's) and GaAs/Si Using Novel Scanning Electron Microscopy Based Techniques

D. H. Rich
University of Southern California, danrich@alnitak.usc.edu

H. T. Lin
University of Southern California

Y. Tang
University of Southern California

K. Rammohan
University of Southern California

A. Larsson
Chalmers University of Technology

Follow this and additional works at: https://digitalcommons.usu.edu/microscopy

Part of the Biology Commons

Recommended Citation

Rich, D. H.; Lin, H. T.; Tang, Y.; Rammohan, K.; and Larsson, A. (1995) "Optical Studies of InGaAs/GaAs Multiple Quantum Wells (MQW's) and GaAs/Si Using Novel Scanning Electron Microscopy Based Techniques," *Scanning Microscopy*: Vol. 1995 : No. 9 , Article 11.
Available at: https://digitalcommons.usu.edu/microscopy/vol1995/iss9/11

This Article is brought to you for free and open access by the Western Dairy Center at DigitalCommons@USU. It has been accepted for inclusion in Scanning Microscopy by an authorized administrator of DigitalCommons@USU. For more information, please contact digitalcommons@usu.edu.

UtahStateUniversity
MERRILL-CAZIER LIBRARY

Scanning Microscopy Supplement 9, 1995 (Pages 131-155) 0892-953X/95$5.00+.25
Scanning Microscopy International, Chicago (AMF O'Hare), IL 60666 USA

OPTICAL STUDIES OF InGaAs/GaAs MULTIPLE QUANTUM WELLS (MQW's) AND GaAs/Si USING NOVEL SCANNING ELECTRON MICROSCOPY BASED TECHNIQUES

D.H. Rich[1*], H.T. Lin[1], Y. Tang[1], K. Rammohan[1] and A. Larsson[2]
[1]Photonic Materials and Devices Laboratory, Department of Materials Science and Engineering
University of Southern California, Los Angeles, CA 90089-0241
[2]Chalmers University of Technology, Department of Optoelectronics and Electrical Measurements
S-412 96 Göteborg Sweden

Abstract

The influence of defects on electron-hole plasma transport in *nipi*-doped $In_{0.2}Ga_{0.8}As/GaAs$ multiple quantum wells (MQWs) has been studied using a novel technique called electron beam induced absorption modulation (EBIA) imaging. Modulation doped MQW structures exhibit large optical nonlinearities and are important for the development of all-optical spatial light modulators used in optical computing and communication. The electron-hole plasma is generated by a high-energy electron beam in a scanning electron microscope and is used as a probe to study the MQW absorption modulation induced locally by the electron beam. The influence of structural defects on the diffusive transport of carriers is imaged with a μm-scale resolution. A strong spatial correlation between dark line defects observed in cathodoluminescence (CL) and absorption modulation steps in EBIA reveals the existence of strain-induced band edge fluctuations that are caused by misfit dislocations. The spatial variation of stress in metalorganic chemical vapor deposition grown GaAs/Si has been studied with linearly polarized cathodoluminescence (LPCL). GaAs grown on Si wafers in selective areas (10 to 1000 μm mesas) were studied. The large difference in thermal expansion coefficient between GaAs and Si results in thermal stress-induced microcracks and dislocations which can occur upon cooling from growth temperatures. Using LPCL, we have determined the spatial distribution of the stress tensor from the polarized CL strain-split peak positions and solutions to the orbital-strain Hamiltonian.

Key Words: Cathodoluminescence, multiple quantum wells, lattice mismatch, thermal stress, misfit dislocations, point defects, nipi doping.

*Address for correspondence:
Daniel H. Rich, address as above.
Telephone number: (213) 740-4329
FAX number: (213) 740-7797
E-mail: danrich@alnitak.usc.edu

Introduction

The steady improvement in the quality of epitaxially grown strained semiconductors has lead to the development of opto-electronic devices that are critical components of optical computing and communication architectures. The use of strained $In_xGa_{1-x}As$ in the active region of quantum well (QW) lasers fabricated on GaAs substrates allows for the utilization of unique advantages due to the modification in electronic structure [34]. The strain-induced splitting of the valence bands results in a lowering of the density of states in the highest energy valence band, thus permitting lasing to occur at a lower threshold current than for unstrained lasers. The attendant lowering of the in-plane hole mass results in a higher speed lasing modulation capability [34]. Likewise, the use of a thin InGaAs film as a channel layer on GaAs in a high electron mobility transistor (HEMT) has enabled significant enhancements in high-speed switching applications owing to a higher electron mobility and increase in the Γ-L conduction band intervalley energy separation [32].

The spatially separated electron-hole plasma that can be generated in periodically doped *nipi* multiple quantum well (MQW) structures exhibits novel electronic and optical properties which can be utilized for applications in photonic devices [4, 15, 23, 29, 30, 31]. Because of large enhancements in the excess carrier lifetime and in-plane ambipolar diffusion constant, large excess carrier concentrations can be created by relatively weak optical excitation to alter the effective *nipi* band gap, MQW excitonic absorption, and refractive index [4, 15, 18, 23, 29, 30, 31]. The InGaAs/GaAs MQW system, when utilizing these photo-optic effects, is a leading candidate for the fabrication of spatial light modulators (SLMs) which are the building blocks of high-information throughput optical computing elements and Fourier-plane image processing devices [17, 36]. SLMs, which modulate the intensity, phase, or polarization of optical signals in space and time, are essential components of optical information processing, digital optical communication, and visual display systems [36]. The incorporation of

nipi-doped MQWs into an asymmetric Fabery-Perot cavity has recently demonstrated the feasibility of high-contrast optically-addressed SLMs [17]. Pixelated SLM architectures allow for a large degree of parallelism and interconnectivity, and can, therefore, serve as basic elements for a variety of neural network and artificial intelligence designs. Applications in real-time image processing, object tracking and pattern recognition require a choice of electro-optic semiconductors materials which are suitable for integration into electronic systems. In particular, SLMs and lasers based on InGaAs/GaAs QWs are attractive since, in a transmission geometry, such SLMs can take advantage of the transparent nature of the GaAs substrate.

Heteroepitaxial GaAs films grown on Si substrate have attracted a great deal of attention in recent years, owing to the possibilities for monolithic integration of electronic and photonic technologies [5, 19, 21, 27, 35, 38]. High-quality heteroepitaxial GaAs/Si growth offers the opportunity of combining the high reliability and accessibility of Si-based microelectronics processing with the high-speed and light-emitting capabilities of GaAs and other III-V alloys. However, such applications are not without some serious material-related problems inhibiting high quality growth. A 4.2% lattice mismatch between GaAs and Si at growth temperature is compensated by dislocations at the interface. The fabrication of hybrid photonic and electronic devices based on InGaAs/GaAs/Si is certainly attractive, yet presents an even greater challenge. The development of the aforementioned applications of the strained InGaAs/GaAs system has supplied the driving force for studies in the fundamental structural and optical properties. The deleterious nature of strain-induced defects such as misfit and threading dislocations and point defects can significantly influence the optical and transport properties. The presence of such defects can create competing recombination channels which can reduce the radiative efficiency of device material and create spatial nonuniformities in the optical properties. The interfacial strain can be driven by either lattice or thermal mismatch or a combination of both. The ratio of the GaAs and Si thermal expansion coefficients is about 2.5 at typical growth temperatures in excess of 700°C; the subsequent cooling to room temperatures results in a large tetragonal distortion which can cause wafer bowing and the formation of microcracks to partially relieve the thermal stress [5, 19, 21, 27, 35, 38]. The residual thermal stress and distribution of microcracking on GaAs/Si will alter the electronic and optical properties, and the effects of stress on the splitting of the j = 3/2 heavy-hole (hh; $m_j = \pm 3/2$) and light-hole (lh; $m_j = \pm 1/2$) bands at **k** = 0 have been studied, and optical transitions involving these states exhibit polarization selection rules which depend on the strain [3, 26].

Experimental Approaches

In order to more fully understand the influence of strain and the associated defects on the optical and structural properties of III-V heteroepitaxial systems, we have employed two novel scanning electron probe techniques. The first is **linearly polarized cathodoluminescence** (LPCL) imaging, which is used to study defect-induced μm-scale variations in the strain tensor for lattice- and thermal-mismatched heterostructure systems [27]. In LPCL, the polarization properties of the luminescence is measured to evaluate the spatial variations in stress and strain tensors. Such variations can occur as a result of strain relaxation near dislocations, cracks, and edges. Recently, we have demonstrated that LPCL imaging and spectroscopy can be a useful tool to study the stress-induced splitting of the j = 3/2 valence bands [27]. In order to more fully understand the ramifications associated with fabricating devices with the GaAs/Si system, it is essential to elucidate in detail the spatial variation in the strain, and a high-spatial resolution technique, such as offered in CL, is needed to locally probe the strain-induced splitting of the j = 3/2 valence bands.

In this study, we find that the stress decay in the vicinity of edges, corners, and microcracks is found to be modeled well with a bi-metal thin film model, showing an approximately exponential decay in stress in GaAs/Si. The in-plane stress tensor comprised of transverse normal ($\sigma_\perp$; perpendicular to the edge) and longitudinal ($\sigma_\|$; parallel to the edge) terms whose relative contributions can be determined from the polarized CL strain-split peak positions and solutions to the orbital-strain Hamiltonian. LPCL imaging is observed to be sensitive to local deviations from biaxial stress and can be used to map the boundaries of stress contours near mesa edges and defects. The GaAs/Si system has also been studied previously with photoluminescence (PL) [19, 35, 38, 40], photoluminescence excitation (PLE) [40], photoreflectance (PR) [5], and CL [19, 21, 27, 35, 38, 41].

Our second new technique is called **electron beam-induced absorption-modulation** (EBIA) imaging, which is used to study the influence of defects on the dynamics of excess carrier recombination and electron-hole plasma transport [29, 30, 31]. In EBIA, an electron-hole plasma is generated by a high-energy electron beam in a scanning electron microscope and is used as a probe to study the MQW absorption modulation induced locally by the electron beam. The influence of structural defects on the diffusive transport of carriers is imaged with a μm-scale resolution. EBIA can be used to discriminate between defect generation that occurs at the MQW-to-GaAs substrate interface and defects which exist in

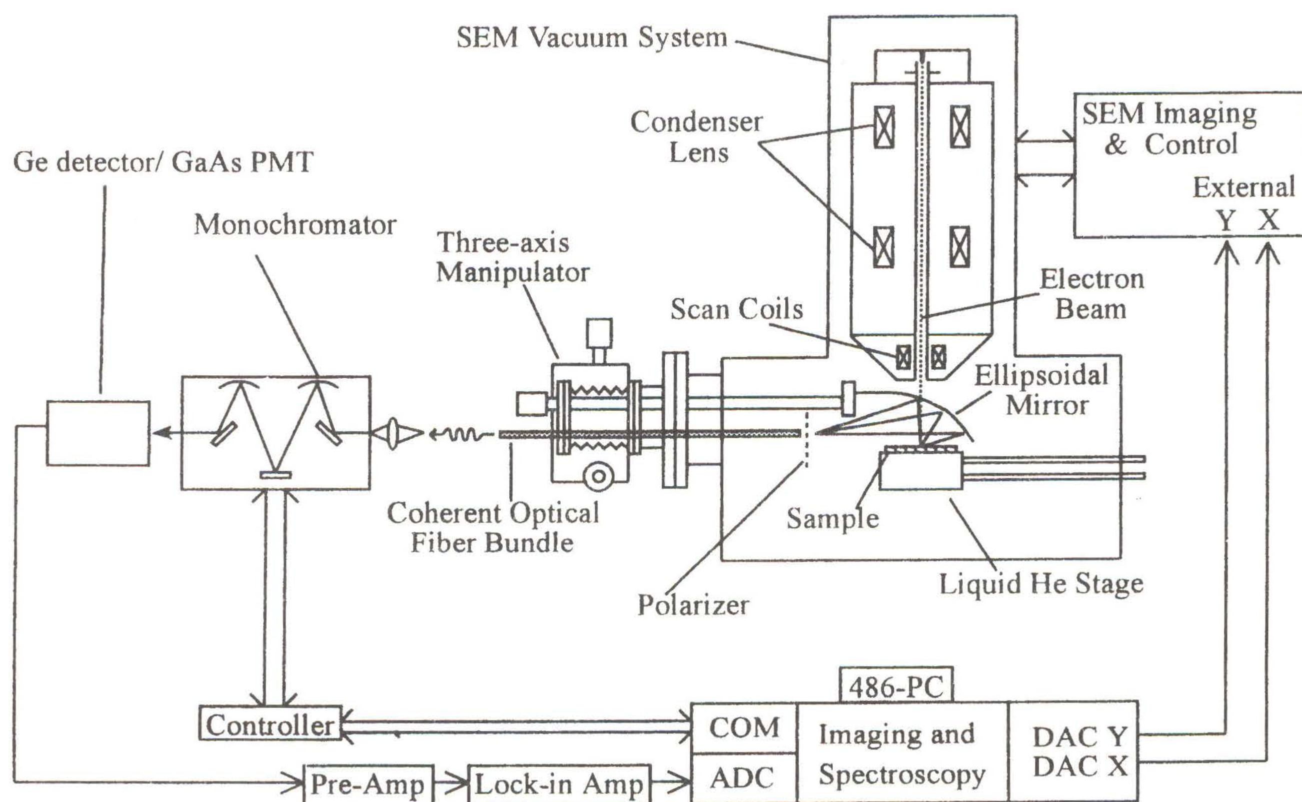

Figure 1. Schematic showing the linearly polarized cathodoluminescence detection system installed on a JEOL-840A SEM. An ellipsoidal mirror is used to collect the luminescence and light is transmitted to the monochromator by a high-resolution coherent (imaging) fiber bundle. The rastering of the electron beam, control of the monochromator, and processing of the images is facilitated by a PC-486 microcomputer.

the MQW region [29, 30]. A strong spatial correlation between dark line defects (DLDs) observed in CL and absorption modulation steps in EBIA reveals the existence of strain-induced band edge fluctuations that are caused by substrate-to-MQW interfacial misfit dislocations. The present results demonstrate that in certain lattice-mismatched heterostructures, a Cottrell atmosphere of point defects separated from interface misfit dislocation cores can affect the lateral transport of carriers. The excess carrier lifetime and diffusion coefficient have been obtained by a one-dimensional Shockley-Haynes type diffusion experiment using EBIA [31].

CL and EBIA instrumentation

Cathodoluminescence measurements were performed with a JEOL 840-A thermionic emission (with both tungsten and LaB_6 filament capabilities) scanning electron microscope (SEM) that is equipped with a 500 kHz band-width electromagnetic beam blanking system. The CL optical collection system and cryogenic specimen stage were designed and constructed at the University of Southern California and a schematic is shown in Figure 1. The luminescence emitted from the sample was collected with an ellipsoidal mirror which focuses the radiation onto a coherent optical fiber bundle leading outside the SEM vacuum chamber to a 0.25 m focal length monochromator. The coherency of the bundle allows for a direct imaging of light at the second ellipsoidal focus into the entrance slit of the monochromator. The bundle acts as an efficient polarization scrambler, and to perform polarization measurements a rotatable vacuum polarizer was mounted directly in front of the bundle. In order to account for polarization mixing effects caused by reflection at the mirror, e.g., due to finite solid angle of collection and changes in the electric field (E) phase and amplitude, a linearly polarized Lambertian (cosine) source was placed at the focus to simulate emission from the sample. The intensity extinction ratio $I_\perp/I_\parallel$, measured by rotating one polarizer 90° with respect to the other, departed from the ideal value of 0 and was found to be $I_\perp/I_\parallel \approx 0.27$. The slit width of the

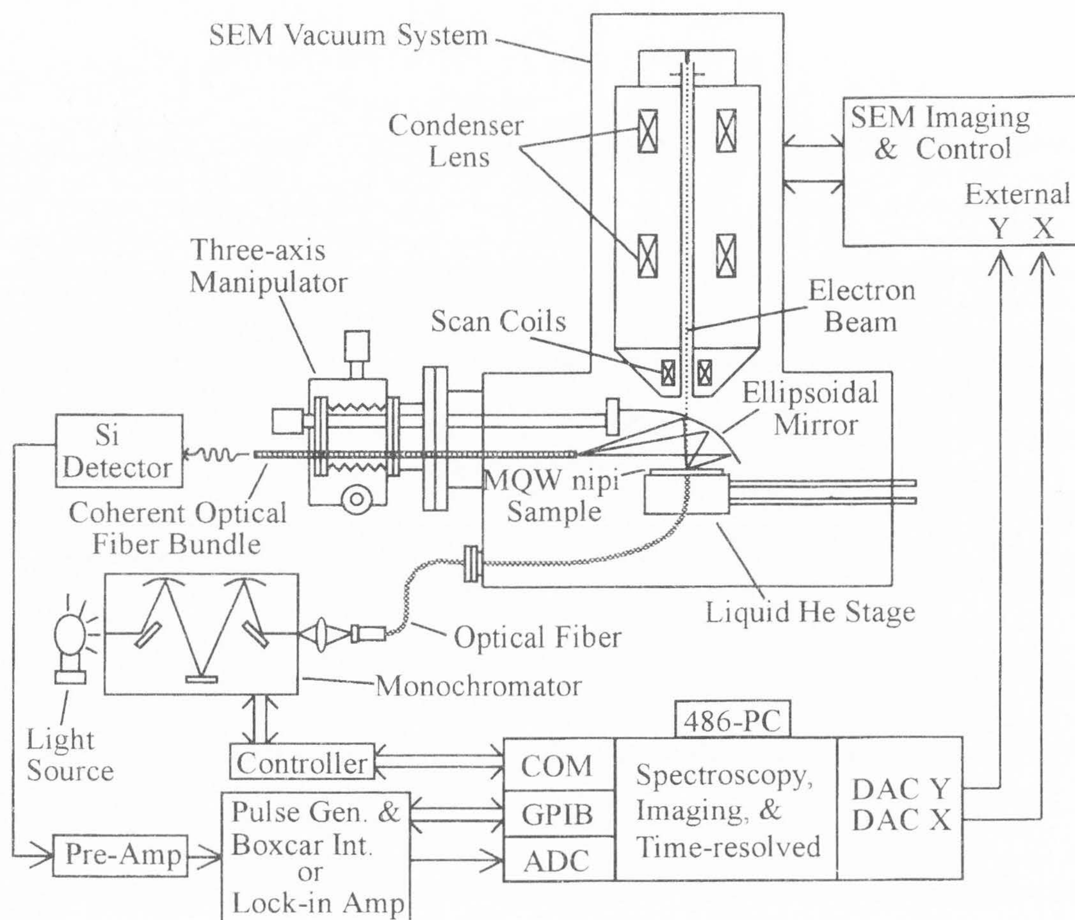

Figure 2. Schematic of the EBIA setup which utilizes the modified CL apparatus shown in Figure 1.

monochromator was chosen to give a spectral resolution of 1 nm. A North Coast liquid nitrogen cooled EO-817 Ge p-i-n detector, a standard non-cooled Si p-i-n detector, and a Hamamatsu Cs:GaAs photomultiplier photon counting system were used to detect the dispersed radiation; this allowed for wavelength detection in the 300 to 1800 nm range. Cryogenic cooling with sample articulation is accomplished by an oxygen-free high-purity Cu braid connection between the Cu sample holder and a High-tran input cold-finger, designed by R.G. Hansen and Associates. The system can be cooled with either liquid helium or liquid nitrogen and allows for a continuous temperature control range between 15 and 350K.

In EBIA, the spatially separated excess carriers in periodically *nipi*-doped samples are generated by the high-energy electron beam within the SEM. The electron probe has the advantage that the electron-hole pair density in the excitation volume is nearly homogenous for appropriate beam energies (i.e., all QW layers can be excited equally). By utilizing the scanning capability of the SEM, spatial imaging information in addition to spectral absorption variations can be obtained. The experimental setup utilizes the cathodoluminescence system of Figure 1 to collect light which is transmitted through the MQW structure as illustrated in Figure 2.

Figure 3 (*on facing page*). Band diagram of a MQW *nipi* structure (sample A) showing spatial separation of electrons and holes which occurs under electron beam excitation in (a). The structure is illustrated for the case of δ-doping, which results in linear variations in the conduction (E_C) and valence (E_V) band edges relative to the quasi Fermi-levels for electrons and holes (ϕ_n and ϕ_p, respectively). The band diagram for the structure of sample B (with an exchange in n- and p-type dopants relative to sample A) is illustrated in (b). The structure of sample C shows the QWs subject to the built-in electric field in the i-layer in (c); changes in the built-in field due to carrier excitation will lead to changes in the quantum confined Stark effect.

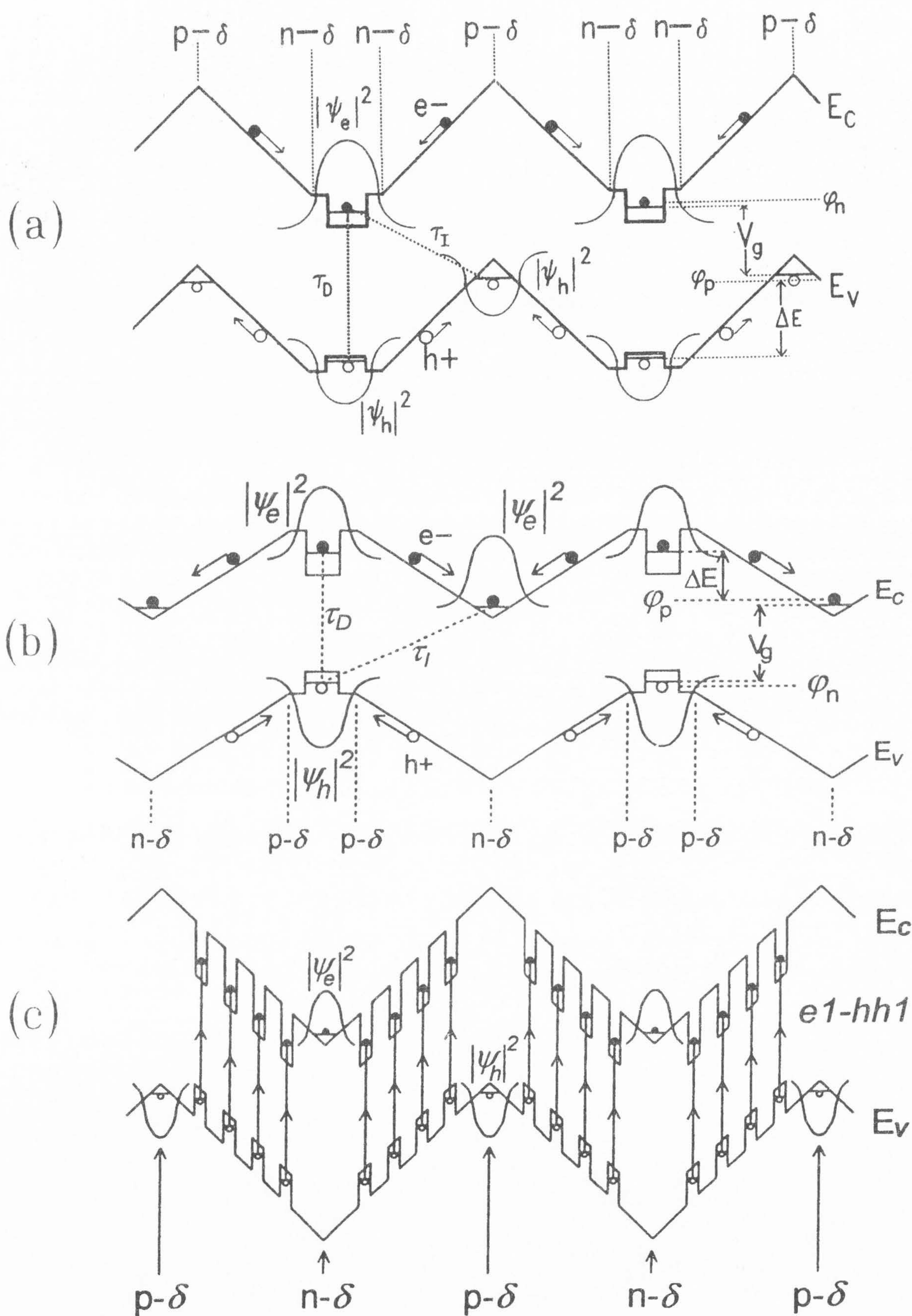
(a)
p-δ
n-δ
n-δ
p-δ
n-δ
n-δ
p-δ
$|\psi_e|^2$
e−
E_C
φ_n
τ_I
V_g
τ_D
$|\psi_h|^2$
φ_p
E_V
ΔE
h+
$|\psi_h|^2$
(b)
$|\psi_e|^2$
e−
$|\psi_e|^2$
ΔE
φ_p
E_C
τ_D
V_g
τ_I
φ_n
$|\psi_h|^2$
h+
E_V
n-δ
p-δ
p-δ
n-δ
p-δ
p-δ
n-δ
(c)
E_C
$|\psi_e|^2$
e1-hh1
$|\psi_h|^2$
E_V
p-δ
n-δ
p-δ
n-δ
p-δ

A multimode optical fiber with a 100 μm core diameter is used to transmit light from a tungsten light source dispersed by a monochromator to the backside of the sample in the SEM vacuum chamber. The technique utilizes lock-in detection by chopping either the light source from the monochromator or the electron beam source. The QW absorption coefficient is dependent on the local excess carrier density in the vicinity of the optical fiber. The images reveal an absorption modulation contrast caused by the influence of intrinsic and extrinsic recombination channels on the diffusion of spatially separated carriers to the position of the optical fiber. That is, the absorption coefficient for light with a wavelength near the first quantized heavy-hole to electron (hh1-e1) excitonic transition energy is dependent on the electron beam position. Lifetime effects and recombination centers can be examined by varying the sample temperature and by modulating the electron beam source to study the carrier dynamics.

Sample Structure and Preparation

The GaAs/Si(001) sample studied was grown at Spire Corporation in an MOCVD reactor with modification for atomic layer epitaxy (ALE) operation using trimethylgallium (TMG) and arsine (AsH_3) [19]. For selective growth, 2-inch, n-type Si wafers oriented 2° off the (001) towards the [110] direction were initially covered with SiO_2 to a thickness 0.5 to 0.6 μm. Using such vicinal Si(001) substrates, the amount of anti-phase disorder in the resulting GaAs film is markedly reduced due to the increased biatomic step density on the vicinal Si surface [14]. Squares with dimensions in the range 10 to 1000 μm, with their edges parallel to the two orthogonal <110> directions, were photolithographically defined on a SiO_2 mask and windows were etched down to the Si substrate. Following an initial high temperature bakeout in H_2, a 100 to 200 Å nucleation layer was deposited by ALE. Conventional growth was then resumed at 650°C until the thickness of GaAs layer reached 1 μm. Finally, the SiO_2 mask was removed by etching in 5% buffered HF and, after which only GaAs square mesas remained on the Si substrate.

The modulation doped *nipi* MQW samples were grown by Molecular Beam Epitaxy (MBE) [15]. Sample A consists of 44 $In_{0.2}Ga_{0.8}As$ QWs, each 65 Å wide, and separated by 780 Å thick GaAs barriers. In the center of each GaAs barrier, a p-type Be-doping plane with a sheet density of 9.0×10^{12} cm^{-2} was inserted. On both sides of the QWs, using 100 Å thick spacer layers, n-type Si-doping planes with a sheet density of 3.0×10^{12} cm^{-2} were inserted. The sample was capped with a 5000 Å undoped GaAs layer. These doping levels give ideally an excess hole concentration and a depletion-induced modulation depth approximately equal to the effective bandgap of the InGaAs QWs. The δ-doping causes a linear variation in the band edges along the growth direction, and the band diagram is shown in Figure 3a for sample A. Sample B is a complementary structure to that of sample A; the structural dimensions are identical except the doping type is reversed. That is, the center of each GaAs barrier contains a n-type Si-doping plane with a sheet density of 9.0×10^{12} cm^{-2} and the sides of the QW contain p-type Be-doping planes of density 3.0×10^{12} cm^{-2} each; the band diagram is illustrated in Figure 3b. Sample C consists of six periods of the δ-doped *nipi* structure whose band diagram is illustrated in Figure 3c. The sheet doping densities used for both n- and p-type planes is 6×10^{12} cm^{-2} and the distance between the doping planes is 1000 Å. The MQW structure was centered between doping planes in the intrinsic region and is comprised of four $In_xGa_{1-x}As$ QWs with nominal composition $x = 0.23$, each 65 Å thick, and separated by 100-Å-thick GaAs barriers. The structure was capped with 1000 Å of undoped GaAs. An important aspect of *nipi*-doped semiconductors is that passivation of the side edges of a mesa is not required to prevent surface recombination of excess carriers since the **majority** carriers (excess electrons and holes in the n- and p-type regions, respectively) are repelled from these edges. During electron-hole pair generation, electrons will be attracted to the n-type regions and holes to the p-type regions, resulting in their spatial separation, as schematically illustrated in Figure 3.

Results and Discussion

Depth-resolved CL imaging of nipi-doped MQWs

In order to better understand the distribution of defects in the growth direction, we have performed a systematic depth-resolved monochromatic CL experiment of sample A. The CL images of Figure 4 were taken with the monochromator tuned to a wavelength of 950 nm, and various electron beam energies (E_b) ranging from 3 to 35 keV were used, as indicated. The first 0.8 μm of sample A was removed by chemical etching in order to remove the strain-induced dislocations occurring at the MQW-to-GaAs capping layer interface. Dark line defects are seen to clearly run along both <110> directions in the CL images. By reducing the beam energy, the CL emission is sampled from regions closer to the surface. The depth resolution in bulk semiconductors is ordinarily limited by the diffusion length of carriers. However, in this *nipi*-doped structure, carriers can not diffuse appreciably in a direction normal to the surface as a result of the spatial separation of electrons and holes. Therefore, *nipi*-doped $In_xGa_{1-x}As$/GaAs MQW samples are ideal candidates for depth-resolved studies

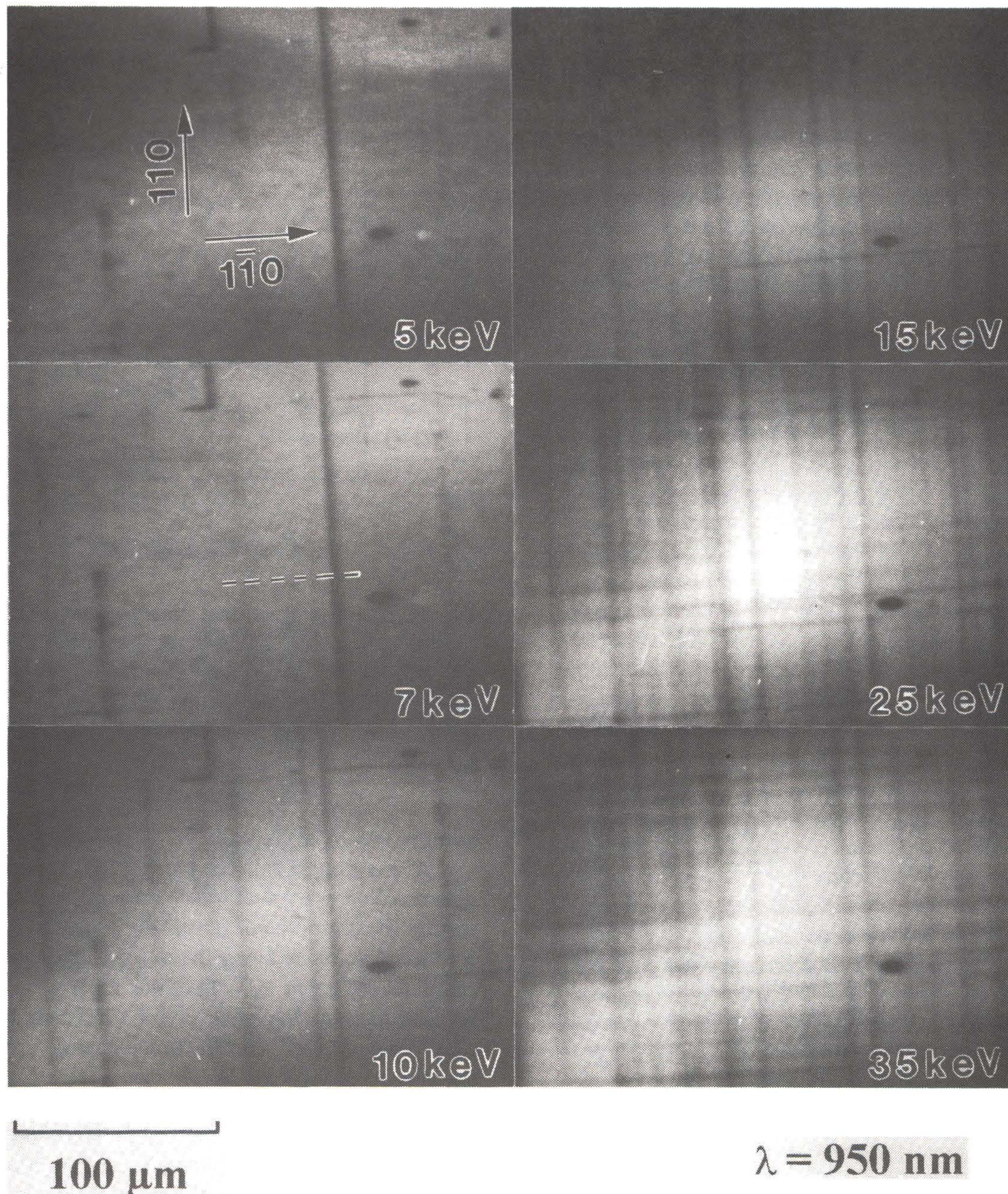

Figure 4. Monochromatic CL images of sample A (λ = 950 nm) taken for various electron beam energies (E_b). The change in DLD contrast with energy reveals the depth dependence of misfit dislocation formation in the MQW.

---

of strain-induced dislocations. In particular, such structures can be used to study the nature of DLDs in MQWs. DLDs can result from nonradiative recombination of minority carriers at the dislocation core [22, 28]. Transmission electron microscopy analysis shows that most of the misfit dislocations are of the 60° type, with the a/2<110> Burgers vector out of the (001) plane [28]. Recent CL data shows that a large portion of the DLD contrast can be caused by the presence of a Cottrell atmosphere of defects that are left in the wake of dislocation propagation and multiplication [28]. As the beam energy is reduced, an increasing anisotropy in the DLD density is observed, with an overall decrease in the total DLD density. For lower beam energies, DLDs are seen to primarily run along the [110] direction. This has previously been attributed to the chemical inequivalence of 60° misfit dislocations possessing like-signs (i.e., having extra-half planes extending in the

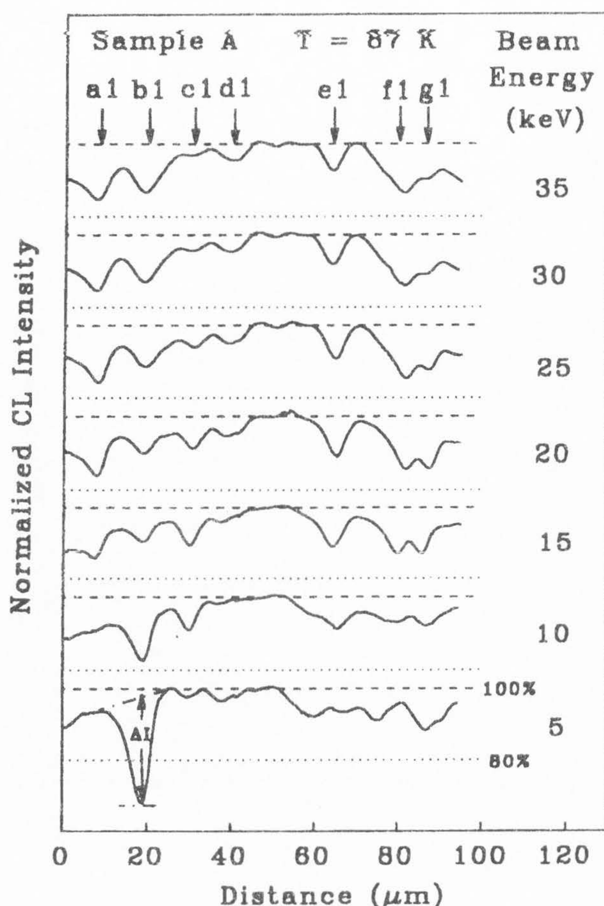

Figure 5. Normalized CL intensity versus distance histogram for the images of Figure 4 at various electron beam energies (E_b). The dashed lines in each of the scans represent an intensity level of 80% relative to the dotted lines. The estimated change in CL intensity, ΔI, caused by a typical DLD is indicated for the 5 keV scan.

same direction with respect to the interface plane) and orthogonal <110> line directions [1]. In the shuffle dislocation set, the extra half-plane terminated with a row of group III and V atoms is referred to as α- and β-type dislocations, and possesses $[1\bar{1}0]$ and [110] line directions, respectively. The anisotropy in α- and β-type dislocation densities may be due to different levels of stress required to generate α and β dislocation cores, and the differences in α and β dislocation propagation velocities [7, 9, 13, 43]. The current data of Figure 4 demonstrates that misfit dislocations can be created in the MQW region, despite the observation that misfit dislocation formation predominantly occurs at the MQW-to-GaAs interfaces [28, 39]. The low density (less than ~ 10^3 cm^{-1}) of misfit dislocations would make detection of misfit in the MQW region in cross-

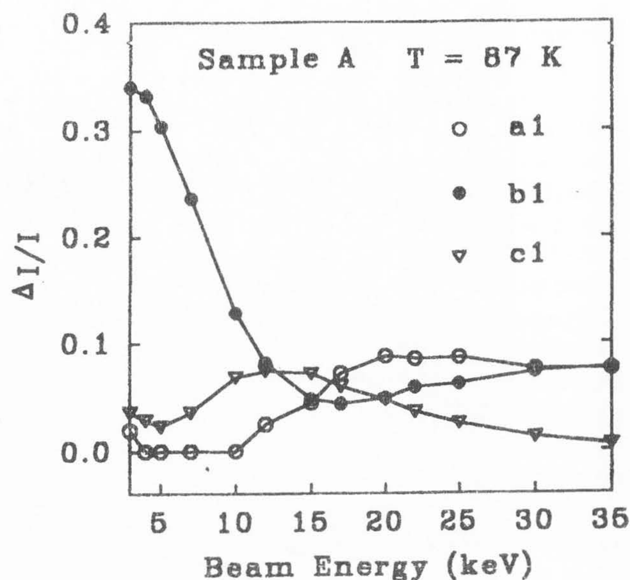

Figure 6. The fractional change in the CL intensity caused by a DLD, $\Delta I/I$, vs. E_b for three DLDs labeled **a1**, **b1**, and **c1** in Figures 4 and 5. The variation in energy dependence shows that DLDs are due to nonradiative recombination occurring at different depths in the MQW.

sectional TEM difficult.

A one-dimensional histogram (CL intensity versus distance line scan) analysis of the images of Figure 4 further illustrates the depth profile of the DLDs. Figure 5 shows line scans along the dashed line shown in Figure 4 for different E_b. The line scans have been normalized to show the same average intensity for regions away from DLDs. The fractional change in the CL intensity caused by a DLD, referred to as $\Delta I/I$, is plotted versus beam energy in Figure 6 for three different DLDs (labeled a1, b1 and c1 in Fig. 5) found in close proximity to each other. As E_b varies from 3 to 20 keV, DLD a1 shows a monotonic increase in $\Delta I/I$, after which $\Delta I/I$ becomes nearly constant for $E_b \gtrsim 20$ keV. DLD b1 shows a decrease in $\Delta I/I$ as E_b increases over the range $3 \leq E_b \lesssim 17$ keV, which is followed by a steady increase in $\Delta I/I$ for $E_b \gtrsim 17$ keV. DLD c1 exhibits an increase in $\Delta I/I$ as E_b increases for $3 \leq E_b \lesssim 12$ keV, followed by a decrease for $E_b \gtrsim 12$ keV. The characteristic dependence of $\Delta I/I$ on E_b evidently reflects the depth in the MQW at which nonradiative recombination gives rise to the DLD. A variation in the beam energy over the range 10 to 40 keV results in a corresponding tenfold increase in the penetration depth (R_e) and the peak position (R_m) of the electron-hole pair density creation function [6]. Theoretical plots of R_m and R_e as a

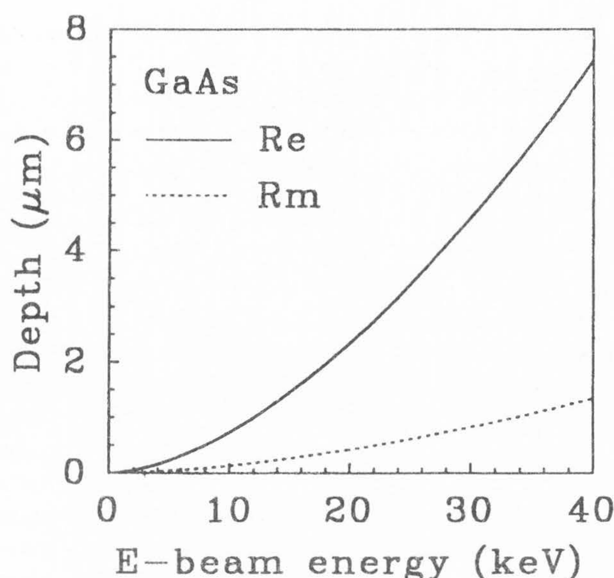

Figure 7. Theoretical plots, based on the model of Everhart and Hoff [6], for the one-dimensional electron-hole pair density maximum peak position (R_m) and the electron penetration range (R_e) as a function of electron beam energy.

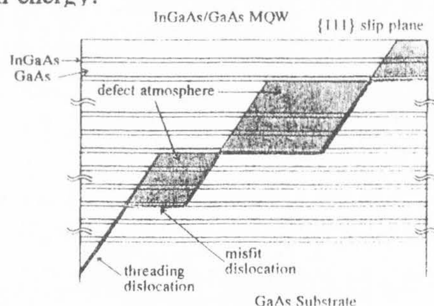

Figure 8. Schematic showing stepping sequence of 60° dislocations in the *nipi*-doped MQW. In this model, the threading dislocation segments elongate (bend over) into misfit dislocations at different stages during MQW growth, leading to the observed depth dependence of DLDs. A Cottrell atmosphere of defects is left in the wake of dislocation propagation (shaded region). The diagram shows a {111} slip plane.

---

function of E_b, from the one-dimensional penetration model of Everhart and Hoff [6], are shown in Figure 7 for an electron beam excitation in GaAs. The position of the onset of DLD contrast, therefore, is given approximately by the theoretical results of Figure 7. DLDs a1 and c1 show an onset in $\Delta I/I$ and imaging contrast when E_b is about 15 and 10 keV, respectively, corresponding to an R_e of 1.5 and 0.7 μm, thereby yielding the approximate position below the surface of the source of nonradiative recombination. DLDs b1 and c1 show an eventual decrease in $\Delta I/I$ that is due to a generation of a larger fraction of carriers in a region deeper (closer to the GaAs substrate) than the position of the region which yields the nonradiative recombination. **We stress that this type of analysis is applicable exclusively for the present nipi-doped structure because diffusion of carriers along the growth direction is negligible.**

In order to better understand the geometrical configuration of misfit dislocations which give rise to the observed behavior in DLDs, we consider the substrate as possessing a fixed number of threading dislocation sources and substrate surface defects and impurities, which act as heterogeneous nucleation sites for 60° threading dislocations in the MQW [7]. Once the thickness of the epilayer, during the InGaAs/GaAs MQW growth, has reached a value where the strain force is equal to the dislocation line tension which resist the elongation of the dislocation, the dislocation will glide laterally on a {111} slip plane, resulting in an interfacial misfit dislocation [2, 24]. The general treatment of Matthews and coworkers have yielded an equilibrium model for determination of heteroepitaxial critical thicknesses [24]. Dislocation elongation is an activated process which is controlled by frictional forces such as the Peierls force [8, 11, 44]. Likewise, the presence of surface steps, Cottrell atmosphere of point defects and impurities can affect the kinetics of glide or climb of the dislocation [8, 11, 44]. These factors, combined with dislocation interactions, affect the length of the misfit segment and the eventual pinning of threading dislocations. Given the observed large variation in DLD segment length, which shows a variations from ~1 to greater than 100 μm, it is plausible that a variety of these dislocation pinning mechanisms are possible.

In order to understand the depth-resolved CL data and develop a simple model, we consider the following arguments. During MBE growth of InGaAs MQWs possessing a large number of QWs, a "critical thickness" will be reach at some intermediate stage of the growth at which misfit dislocation elongation will occur. At this point, the final structure is incomplete and subsequent growth over a region containing a pinned threading dislocation will again reach a thickness at which in-plane elongation of the dislocation will again proceed. The result is a step-like sequence of misfit and threading dislocation segments, as schematically illustrated in Figure 8. This model is intuitively based on the CL imaging results which show marked variations in the depth of DLD sources. As we have previously argued, the Cottrell atmosphere of point defects generated in the wake of the gliding threading segments will contribute to the nonradiative contrast in the vicinity of the dislocation cores. Since the glide of threading segments will affect the material above the current step location, this model

predicts that material below the misfit segment will be free of such nonradiative sources. The experimental results are consistent with this prediction since an increase in the beam energy (and probing depth) results in a reduced contribution to the DLD contrast. A similar stepping sequence has been suggested by Wang, Steeds, and Wolf [39] for misfit and threading dislocations in an InGaAs/GaAs MQW sample possessing a variable QW thicknesses.

EBIA Imaging and Spectroscopy of nipi-doped InGaAs/GaAs MQWs

The modulation of the absorption coefficient in the MQW samples occurs as a result of two different fundamental mechanisms: (i) filling of QW states [15, 18, 23, 29, 30, 31] and (ii) the quantum confined Stark effect (QCSE) [16, 23, 25]. In the structures of samples A and B (see Figs. 3a and 3b), the periodic modulation in the band edges relative to the Fermi-level (or quasi-Fermi levels under excitation) causes electrons and holes to accumulate in the n- and p-type regions, respectively, resulting in their spatial separation. If the structure is designed so that the QWs are placed in the n- or p-type regions, then carriers of one type will fill the QWs and thereby cause a reduction in the absorption coefficient due to (a) screening of the electron-hole Coulombic interaction and (b) band filling of the QW states which reduces the available phase space for absorption at the hh1-e1 excitonic transition energy. The latter effect (b) is analogous to the Burstein-Moss band filling effects in bulk semiconductors.

If, on the other hand, the structure is designed so that the QWs are placed in the i-layers of the *nipi* structure, the QWs under zero excitation are subject to a large built-in electric field due to the periodic doping, as shown in Figure 3c. The QW states are shifted towards lower energies (and lower electron-hole interband transition energy) relative to the case where the same QWs are placed in a homogeneously doped semiconductor; this is a result of the much-studied QCSE [16, 23, 25]. The accumulation of carriers in the n- and p-type regions of the structure of Figure 3c results in a reduction of the built-in field; the amount of the electric field reduction varies logarithmically with the excitation power [16, 18, 23, 30]. This field reduction will shift the QW states towards higher energies, thereby causing a shift in the QW absorption coefficient relative to the unexcited state [16, 23].

In sample A (Fig. 3a), electron-hole pair generation results in electrons accumulating in the QWs while holes accumulate in the region between the wells. This increase in the QW electron density will screen the Coulombic interaction of the QW exciton, resulting in a decreased hh1-e1 excitonic absorption as the excess carrier density increases. The recombination of the spatially separated carriers occurs through spatially indirect radiative tunneling recombination and spatially direct recombination of thermally excited carriers, as denoted schematically by the lifetimes τ_I and τ_D, respectively, in Figure 3a [18, 30]. Absorption spectra (solid lines) for various electron beam currents, I_b, are shown in Figure 9 at a sample temperature of 300K, and were obtained by chopping the monochromator probe. The effective QW absorption coefficients were calculated according to $(-L_{eff})^{-1}\ln T$, where T is the measured normalized transmission through the sample and L_{eff} is the total thickness of the MQW structure [15]. The total light power through the fiber was ~ 10^{-7} W with a spectral resolution of 1 nm. The hh1-e1 exciton peak, which is located at λ = 996 nm, is seen to quench as the current is increased as a result of the increased excess carrier density. The differential absorption spectrum (dashed curve of Fig. 9) was obtained by chopping the electron beam; this enables an observation of the higher lying excitonic transitions. A similar behavior is observed for sample B in Figure 10, where the screening of the hh1-e1 excitonic transitions results from the filling of holes in the QWs. The peak absorption at the exciton resonance, α_{max}, is related to the two-dimensional carrier density in the QW, δn_q, by the expression [15]

$$\alpha_{max} = \alpha_O(1 + \delta n_q / n_{sat})^{-1} \qquad (1)$$

where α_O is the absorption coefficient in the absence of excitation and n_{sat} is the saturation carrier density which was found to be ~ $1\times10^{11}\mathrm{cm}^{-2}$ from optically induced absorption modulation measurements [15]. A greater energy shift δE in the QW intervalence band absorption edge for a given excess carrier density is expected for the structure of sample A since the rate of phase-space filling of states, $\delta E/\delta n_q$, is greater for the conduction band QWs. This rate is given by

$$\frac{\delta E}{\delta n_q} = \frac{h^2}{4\pi m_q} \qquad (2)$$

where m_q is the effective carrier mass and h is Planck's constant. The QW effective masses of electrons and holes are $0.058m_o$ and $0.35m_o$ at a 20% In composition. These masses were taken from a linear interpolation of GaAs and InAs values; m_o is the rest mass of the electron. Using eq. (2), this results in $\delta E/\delta n_q$ rates of 4.1 meV/(10^{11} cm^{-2}) and 0.69 meV/(10^{11} cm^{-2}) for conduction and valence band states, respectively. The data for samples A and B (Figs. 9 and 10, respectively) show that the change in absorption, for a given beam current,

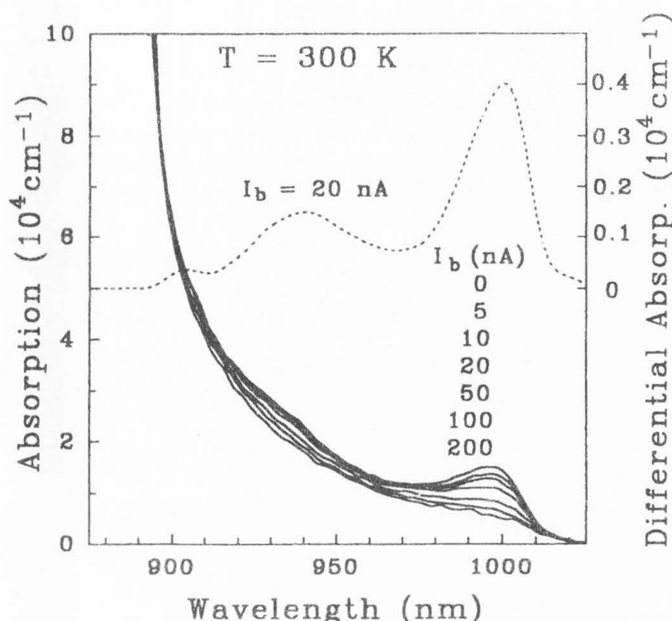

Figure 9. EBIA spectroscopy of sample A at room temperature. The electron beam was focused on a region above the center of the optical fiber. Beam currents (I_b) are indicated. The electron beam-induced absorption changes are caused by band filling and quenching of the hh1-e1 exciton. Differential EBIA spectroscopy measurements (dashed lines) are obtained by blanking the electron beam source.

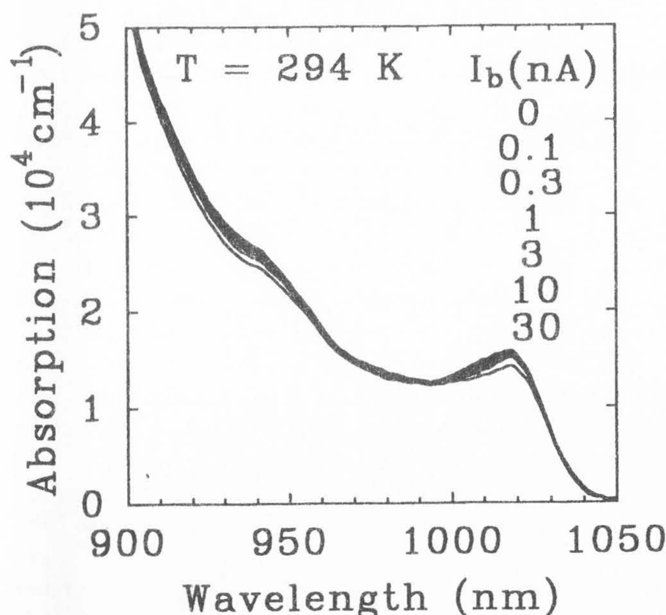

Figure 10. EBIA spectroscopy of sample B at room temperature performed in the same manner as the measurements for sample A in Figure 9.

is greater for the case of sample A, which involves filling of electron states in the QWs. However, a precise measurement of δE from the spectra is not possible, due to the large excitonic line width of ~ 20 meV.

It is possible to obtain spatial information concerning changes in the differential absorption, $\Delta\alpha$, by scanning the electron beam within the vicinity of the optical fiber center. An EBIA image (shown in Fig. 11 for T = 115K), was obtained by detecting the transmitted signal at λ = 950 nm, corresponding to the hh1-e1 exciton absorption. The electron beam (I_b = 1 nA) was pulsed at a frequency of 500 Hz while rastered in 2-dimensions across the sample to generate a 640 x 480 pixel image with the $\Delta\alpha$ intensity value stored in one byte of memory per pixel. The EBIA image shows the influence of structural defects on the diffusive transport of carriers with a μm-scale resolution. The center of the bright spot in Figure 11 corresponds to the region of greatest excess carrier density and the region where the electron beam causes the largest transmission modulation, which is near the center of the optical fiber. The differential absorption, for a beam position fixed at the fiber center, decays exponentially with frequency for frequencies greater than the 3 dB cut-off frequency, f_c, which is ~ 100 Hz for the sample temperature of 115K here [30]. The image has been normalized so that the maximum and minimum $\Delta\alpha$ correspond to the limits of the grey scale. For the case of ambipolar diffusion in one-dimension in this *nipi* MQW structure, an analytical solution showing the absorption modulation as a function of distance and frequency has been determined [31]. The sharp changes in contrast seen as steps in $\Delta\alpha$ have well-defined boundaries along the <110> directions and correlate with DLD orientations as seen in Figure 4. These images further illustrate that the locally generated electron-hole plasma can be used as a probe to study the influence of structural defects on transport since a change in $\Delta\alpha$ is due to defect-induced barriers impeding plasma transport to the fiber center.

A histogram of the imaging results of Figure 11 is presented in Figure 12. The curves illustrate the intensity versus electron beam position relative to the fiber center (distance = 0) along the [110]-oriented line shown in Figure 11 for CL, the absorption modulation $\Delta\alpha$, and its derivative $\partial\Delta\alpha/\partial x$. The center of the steps in $\Delta\alpha$ show up as peaks in the derivative scan. Vertical dotted lines are drawn in the figure to illustrate the strong correlation between dips and shoulders in the CL intensity at DLDs and the positions of the steps observed in the absorption modulation. These results demonstrate, remarkably, that the orientation and positions of steps seen in the absorption modulation correspond with the orientation and position of DLDs seen in the CL image. A previous studied showed that an asymmetry in the DLD density is

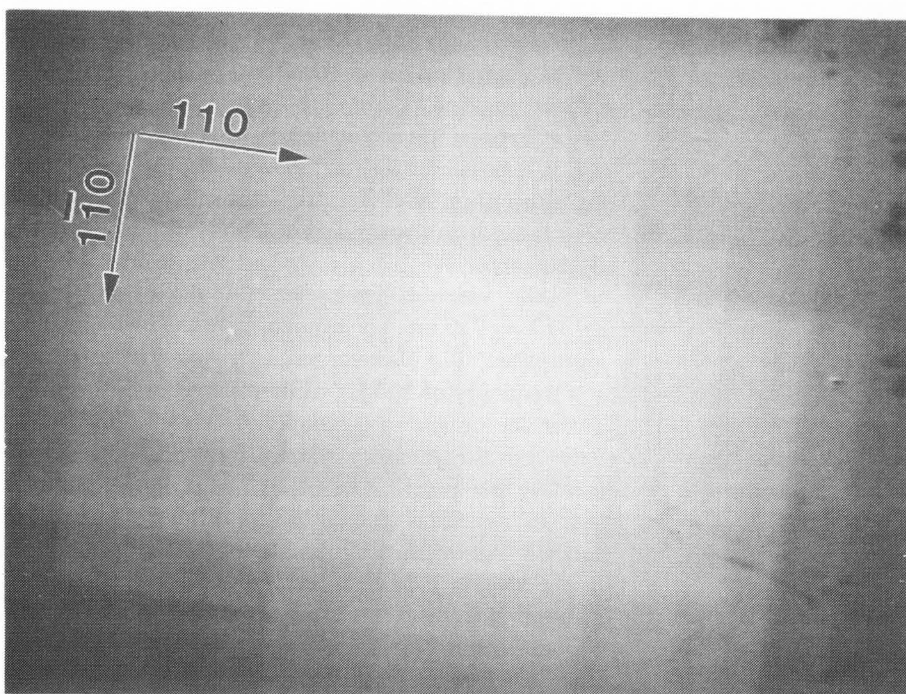

Figure 11. EBIA image of sample A. Sharp changes in contrast (Intensity steps) are observed for $\Delta\alpha$. These steps are seen to spatially correlate with orientation and position of DLDs seen in the CL images of Figure 4. The grey-scale is a representation of the magnitude of $\Delta\alpha$.

correlated with an anisotropy in the ambipolar diffusive transport of the plasma [31].

An EBIA image taken of sample B, at T = 87K, is shown in Figure 13a with the monochromator probe set to λ = 957 nm. A 35 keV beam energy and 10 nA beam current with a 500 Hz beam blanking frequency was used. Unlike the previous image (Fig. 11) of sample A, discrete changes in $\Delta\alpha$ are not observed and the image reveals a cylindrically symmetric contrast in the imaging of $\Delta\alpha$. The CL image of sample B, taken over the same sample region, is shown in Figure 13b. The apparent absence of DLDs in this image illustrates that little relaxation in this structure has occurred. The EBIA images thus reveal that the transport of the electron-hole plasma to the fiber is not impeded, as there is a marked reduction in the DLD density in this sample. These two samples were grown in two different chambers, and slight differences in the growth parameters (e.g. temperature, growth rate, and III-V flux ratios,) would effect the kinetics of dislocation generation. Additionally, the EBIA spectra of samples A and B (Figs. 9 and 10) show a ~ 20 nm (24 meV) shift in the hh1-e1 peak position, indicating that the In composition and/or QW thickness may be different.

EBIA absorption and differential absorption spectra at room temperature, for sample C, are shown in Figure 14. The peak of the absorption spectrum is the hh1-e1 excitonic transition. With increased electron beam current, the transition energy shifts toward shorter wavelengths, indicating that the built-in electric field experienced by the MQWs decreases due to screening of charge in the doping planes by the accumulation of excess carriers [23]. A QCSE occurs here as a result of the field-induced change in quantized electron and hole energy levels [16, 23, 25]. For higher fields (reduced currents), the excitonic resonance broadens and its peak strength is reduced due to a reduced overlap of electron and hole wavefunctions and an increased field-induced tunneling rate of carriers out of the QWs. The differential absorption ($\Delta\alpha$) in Figure 14 was obtained by chopping the electron probe at a low frequency of 5 Hz while keeping the monochromator source unchopped. The peak in the α spectrum is the hh1-e1 excitonic peak position, while the maximum and minimum values in the $\Delta\alpha$ spectrum represent two different excitonic peaks due to the subtraction of beam-on and beam-off absorption spectra.

Two types of EBIA images, at a temperature of 86K, are shown for sample C in Figures 15a and 15b. A beam energy of 30 keV and current of 0.3 nA were used. The image of Figure 15a represents the integrated intensity of all positive $\Delta\alpha$, in the range from 955 $\leq \lambda \leq$ 975 nm, as a function of electron beam position (x,y). This was accomplished by summing 22 discrete monochromatic EBIA images from 955 to 975 nm. A clear contrast due to the strain-induced misfit dislocation

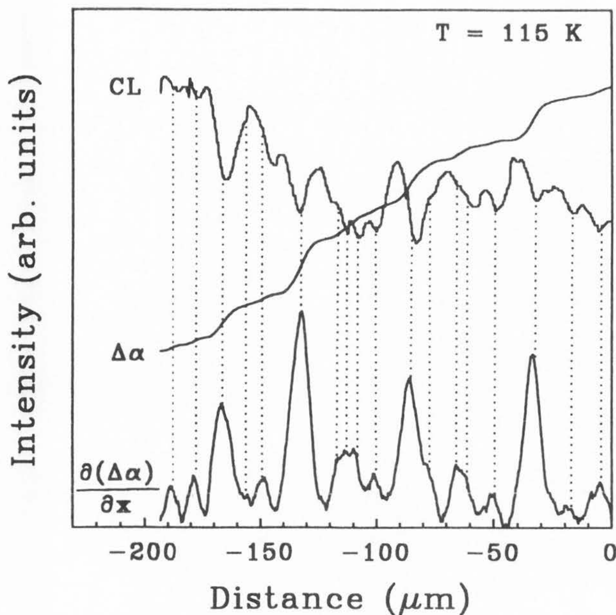

Figure 12. Histograms (intensity versus position) of CL, absorption modulation ($\Delta\alpha$), and its derivative $\partial\Delta\alpha/\partial x$ as a function of the distance (x) from the center of the optical fiber along [110]. The center of the steps in the absorption modulation (peaks in the derivative) are seen to correlate strongly with the minima and shoulders seen in the CL line scan. The minima in the CL scans correspond to the dark line defect positions seen in the CL image of Figure 4.

formation is observed. The region of greatest intensity (white) corresponds to the position of the fiber where $\Delta\alpha$ is the largest. Rectangularly shaped steps in the $\Delta\alpha$ image correlate with the position and orientation of the DLD pattern imaged in the panchromatic CL image of the same region in Figure 15c. A new type of EBIA image is displayed in Figure 15b in which the grey scale key represents a wavelength mapping of the spatial distribution of the high-energy $\Delta\alpha$ peak position. The peak in $\Delta\alpha$ was determined from a 22-point local EBIA $\Delta\alpha$ spectrum for each of the 640 x 480 discrete (x,y) positions in the image. This was enabled by acquiring and processing 22 discrete monochromatic EBIA $\Delta\alpha$ intensity images in the range $955 \leq \lambda \leq 975$ nm. The image clearly reveals the spatial distribution of the QCSE. When the electron beam is positioned at the optical fiber center, the reduction in the built-in field is the greatest, resulting in the largest blue shift (high-energy shift relative to the unexcited sample) of the hh1-e1 transition energy. When the beam is positioned far from the fiber, the shift toward higher hh1-e1 energies is minimized. Figure 16 shows one-dimensional histograms of the

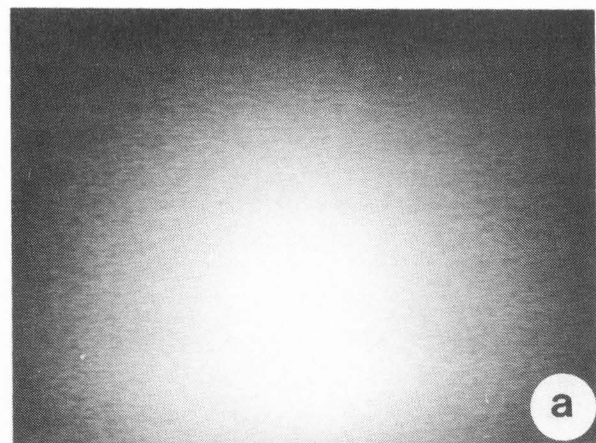

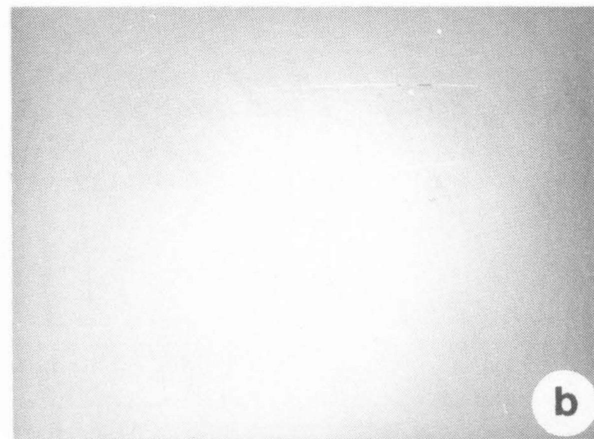

Figure 13. EBIA image of sample B in (a) and a panchromatic CL image in (b) over the same region. A cylindrically symmetric patterned is observed without steps in $\Delta\alpha$, indicating that the influence of defects on transport is reduced compared to that of sample A. In the CL image of (b), the region exhibits little DLD contrast and is consistent with the EBIA image of (a).

hh1-e1 transition energy, the CL DLD contrast, $\Delta\alpha$ and $\partial\Delta\alpha/\partial x$. Regions of maximum change in hh1-e1 transition energy are correlated with DLDs in the CL scan (dips in the line scan) and peaks and dips in $\partial\Delta\alpha/\partial x$, similar to behavior of sample A seen in Figure 12. An asymmetry in the spatial distribution of $\Delta\alpha$ is seen in Figures 15a and 15b._ The regions of largest blue shift are seen along the [110] direction vertically above and below the optical fiber where the image shows light

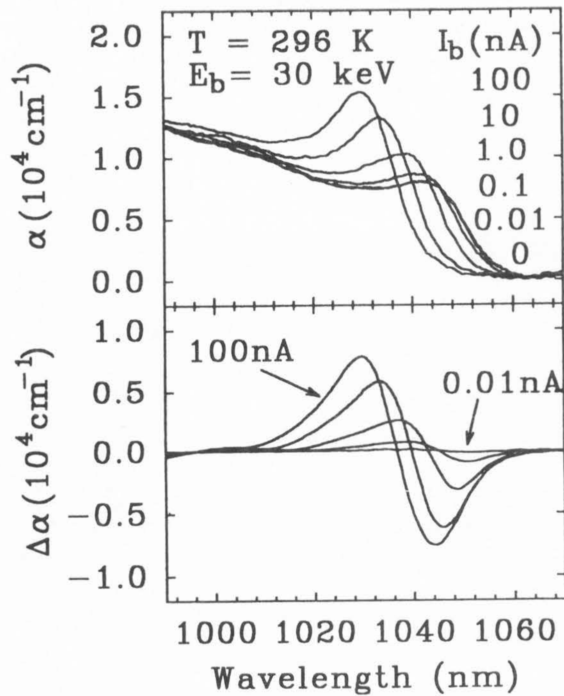

Figure 14. EBIA absorption (α) and differential absorption $\Delta\alpha$ spectra for sample C. The change in the quantum confined Stark effect (QCSE) is observed as the hh1-e1 transition energy shifts to higher energies as the beam current (I_b) increases, indicating the built-in electric field reduces. A reduction in the field induced broadening of the hh1-e1 excitonic transition can be observed for higher beam currents.

Figure 15 (*right column*). EBIA and CL images of sample C. An EBIA image showing the integrated values of positive $\Delta\alpha$ in the range $955 \leq \lambda \leq 975$ nm is shown in (**a**). A new type of EBIA image is displayed in (**b**) in which the grey-scale key represents a wavelength mapping of the spatial distribution of the high-energy $\Delta\alpha$ peak position. The CL image in (**c**) shows the DLD network caused by the formation of misfit dislocations.

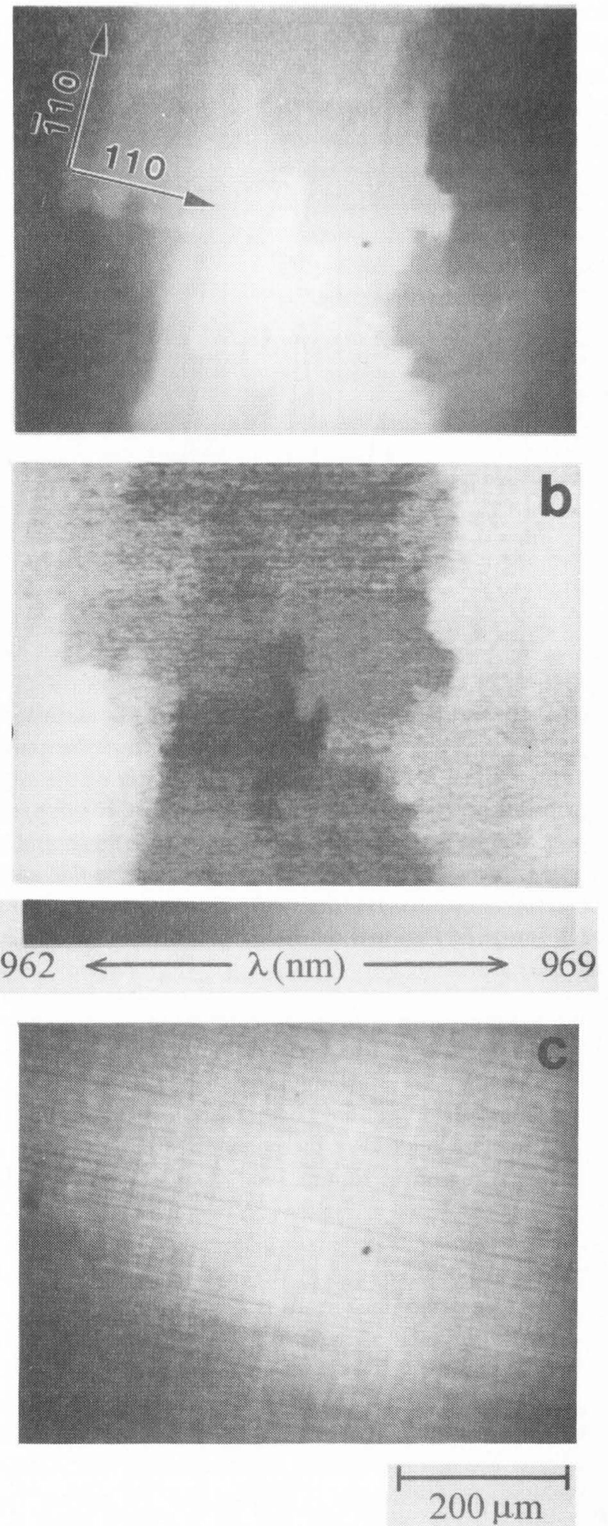

---

grey and white. This behavior is indicative of anisotropic transport of the plasma due to the asymmetry in misfit dislocations as discussed in the case for sample A using depth-resolved CL. The plasma transport is least impeded by defects when the electron beam is positioned along the [$1\bar{1}0$] direction relative to the fiber, thereby enabling a maximum blue shift in the hh1-e1 exciton. This anisotropy in the ambipolar diffusion coefficient has been quantified for the case of sample A [31]. This EBIA imaging represents a new method for visualizing spatial variations in the QCSE and defect induced anisotropy in plasma transport.

Thermal stress in patterned GaAs/Si

The residual thermal stress of GaAs/Si will alter the

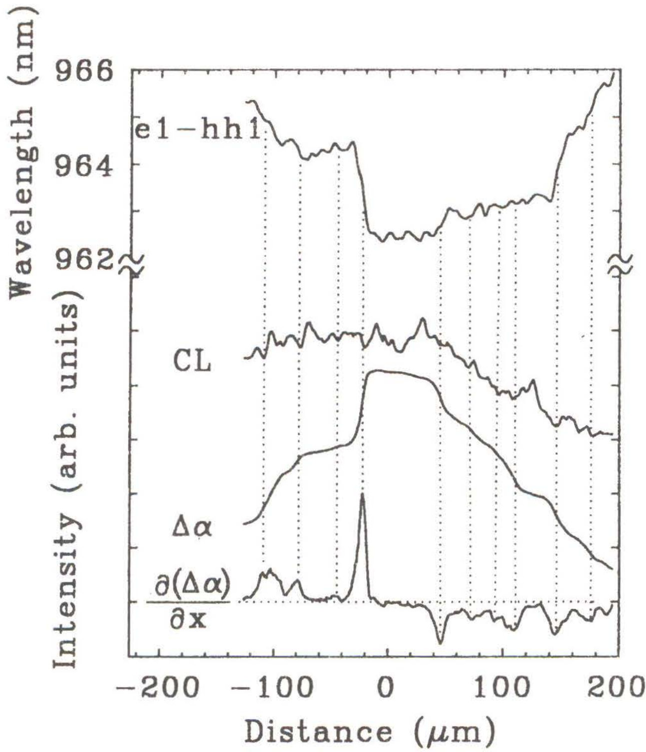

Figure 16. Histograms of EBIA and CL of the imaging data for sample C. The local minima (DLDs) in the CL intensity vs. distance line scan are seen to correlate with the positions of steps in $\Delta\alpha$, peaks in its derivative $\partial\Delta\alpha/\partial x$, and shifts in the e1-hh1 wavelength scan (see Fig. 15b). These results indicate that strain-induced defects will impede e-h plasma transport and cause local variations in the QCSE.

----

electronic and optical properties. The initial lattice mismatch of 4.2% between GaAs and Si results in the nucleation of a large density of misfit and threading dislocations during growth to accommodate the lattice mismatch which would lead to a compressive biaxial stress in the GaAs epilayer in the absence of relaxation. Due to the enhanced thermal expansion coefficient (by a factor of ~ 2.5 at a 700 °C growth temperature) of GaAs relative to Si, the resulting contraction of the GaAs film relative to the Si substrate will cause an in-plane biaxial tensile stress in regions not containing cracks and edges. This tensile stress can eventually lead to the formation of <110> oriented microcracks after cooling [5, 19, 27, 35, 38, 41]. The quantitative effects of a general stress on the splitting of the j = 3/2 hh and lh bands at k = 0 have been previously studied by Pollak and Cardona [26]. Previous studies on the effect of stress on band structure gave the relation between the transition energies and the stress tensor σ [3, 26, 27]. Briefly, the relationship between the orthogonal in-plane stress tensor components, $\sigma_\parallel$ and $\sigma_\perp$, and the energy positions of the strain split peaks can be found by determining the resulting strain tensor ϵ_{km} from the elastic constant tensor C_{ijkm}, using the generalized Hooke's law formalism (i.e., $\sigma_{ij} = C_{ijkm}\epsilon_{km}$) and diagonalizing the orbital-strain Hamiltonian to find the energy eigenvalues [26]. The result for the special case of having two orthogonal in-plane stress components, $\sigma_\parallel$ and $\sigma_\perp$ (both defined with respect to <110> directions), a peeling stress (transverse normal and parallel to the growth direction) [37], σ_z, and a shear stress [37], τ, in GaAs, is

$$E_\pm = E(0) - A(\sigma_\parallel + \sigma_\perp + \sigma_z) \pm \left\{B^2(\sigma_\parallel + \sigma_\perp - 2\sigma_z)^2 + C^2[(\sigma_\parallel - \sigma_\perp)^2 + 4\tau^2]\right\}^{\frac{1}{2}} \quad (3)$$

where $E_\pm$ are the two stress-split transition energies, E(0) is the transition energy in absence of stress. The shear term τ is defined with respect to the <110> directions and, when present, results in tangential components of opposing forces along the GaAs/Si interface and GaAs surface. The constants A, B and C are related to deformation potentials of GaAs and are $A = a(S_{11}+2S_{12})$, $B = b(S_{11}-S_{12})/2$, and $C = dS_{44}/4$, where a is the hydrostatic pressure deformation potential, b and d are uniaxial deformation potentials associated with strains of tetragonal and rhombohedral symmetries, and S_{ij} are elastic compliance constants which form the inverse of the elastic constant tensor. Using the data from the piezo-electroreflectance measurement of Pollak and Cardona [26], we have A = 3.8, B = 1.5 and C = 2.3 meV/kbar. Given the energies of the two strain-split excitonic transitions, we can now determine the local stress tensor based on this equation for regions sufficiently far from the mesa edges, where σ_z and τ are both expected to approach zero [37]. For the biaxial stress case, $\sigma_\parallel = \sigma_\perp$, and the splitting is $4B\sigma$. Under uniaxial stress, the splitting becomes $2(B^2+C^2)^{1/2}\sigma_\parallel$ with the usual assumption of $\sigma_z = \tau = 0$ [21, 26, 27, 35].

Figure 17 illustrates qualitatively the behavior of the valence bands in GaAs subject to uniaxial and biaxial tensile stresses, with respect to the high-symmetry directions that are indicated. The application of a tensile stress will cause a narrowing of the fundamental bandgap and a splitting of the j = 3/2 valence bands. In the absence of a stress, the hh and lh valence bands are degenerate at k = 0. By examining the orbital-strain Hamiltonian matrix [26], the following can be shown: (1) In the representation referred to <001>, the lh and hh wavefunctions will not mix in the strain split j = 3/2 bands for $\sigma_\parallel = \sigma_\perp > 0$ (biaxial stress); (2) In the representation referred to <001>, the lh and hh wavefunctions will also not mix for $\sigma_\parallel > 0$ and $\sigma_\perp = 0$

GaAs

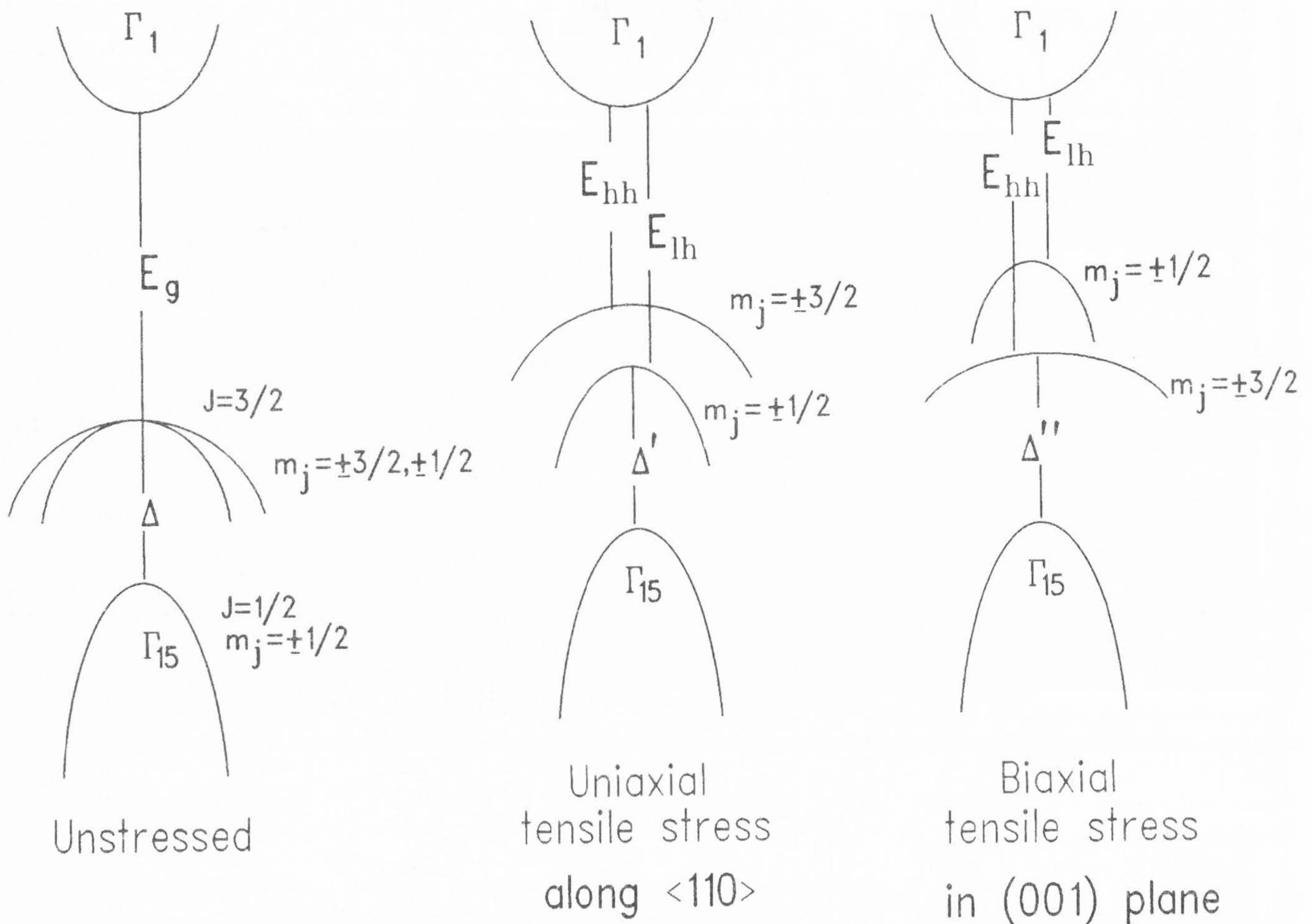

Figure 17. A diagram showing qualitatively the effect of a uniaxial tensile stress on the GaAs valence band structure near **k** = 0 for the cases of uniaxial and biaxial stresses.

(uniaxial stress); (3) In the representation referred to <011>, the lh and hh wavefunctions generally mix for $\sigma_{\parallel} > 0$ and $\sigma_{\perp} = 0$ (uniaxial stress), but the mixing is negligibly small for GaAs; (4) In both <011> and <001> representations, lh and hh wavefunctions can measurably mix in the more general case when $\sigma_{\parallel} > \sigma_{\perp} > 0$. A further consequence, as illustrated in Figure 17 (from the results of eq. (3)), is that for a uniaxial <011> or <001> stress, the hh band is higher in energy than the lh band; this energy order is reversed for a <001> biaxial stress. The understanding of the characters of the valence band wavefunctions that are involved in the excitonic luminescence is an important prerequisite towards identification of the form of the stress tensor and its spatial distribution [27].

Linearly-Polarized CL Spectroscopy of Patterned GaAs/Si(001)

We have examined the effect of pattern size on the biaxial stress. Polarized CL spectra were taken with the electron beam fixed at the center of the square-patterned mesa for various mesa sizes, as shown in Figure 18. The spectra were taken with the polarizer set to detect emission for **E**⊥[110] and **E**‖[110], where the mesa edges are aligned with respect to the <110> directions. A distinct peak with a single shoulder at higher photon energies is observed in all the CL spectra of Figure 18. These two peaks can be decomposed into two excitonic

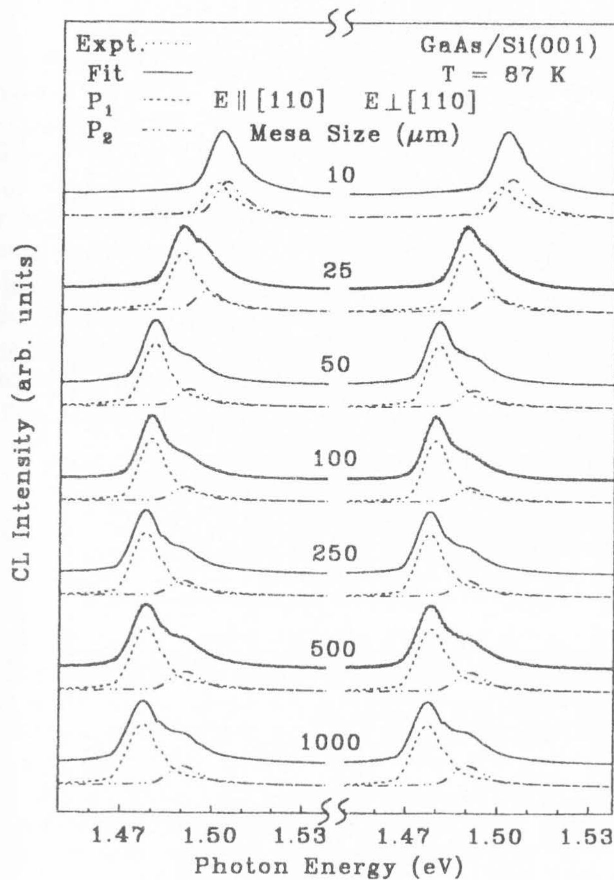

Figure 18. Local cathodoluminescence spectra taken at the centers of square mesas of GaAs on Si. Mesa sizes are indicated in the figure. The decomposition of the luminescence lineshape into two components (labeled as P_1 and P_2) resulting from the strain-induced splitting of the top valence bands is shown. The overall fit to the data is indicated by a solid line running through the data.

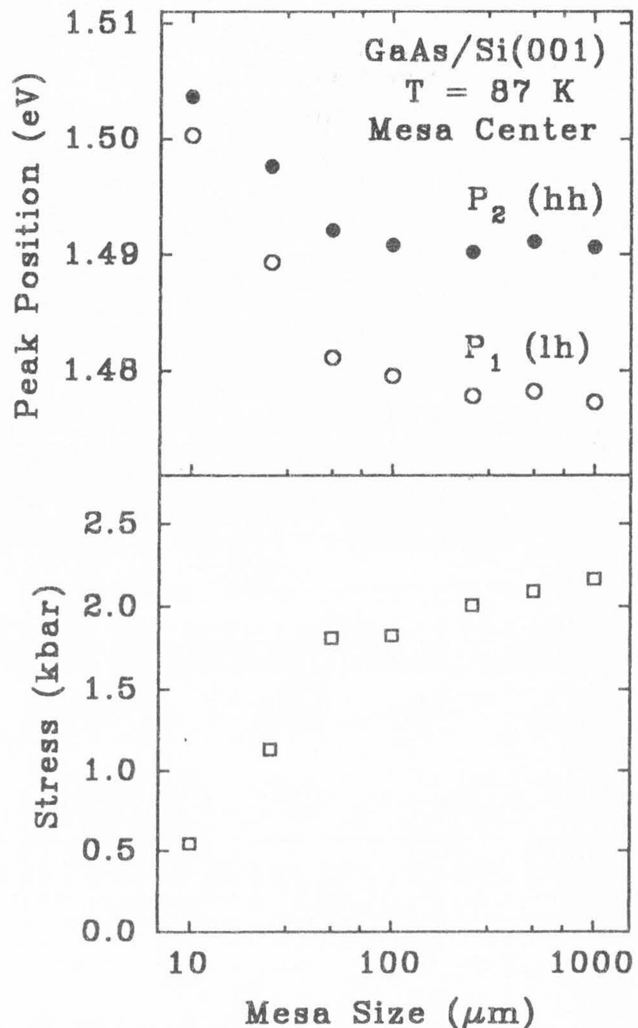

Figure 19. Results of the fits of Figure 18 showing the energy positions of P_1 and P_2 and the biaxial stress calculated from eq. (3), both as a function of mesa size.

transition features resulting from the strain-induced splitting of the j = 3/2 valence bands. The model for the decomposition and the fitting procedure has been previously described [27]. From the fits, the intensity and energy position of each component can be determined. The results of the fits are indicated by the solid lines running through the data points and the decomposed strain split components, labeled P_1 and P_2, are shown offset below the spectra. The spectra of Figure 18 show that the lineshape is insensitive to the polarizer orientation, as the detected emissions with $\mathbf{E} \perp [110]$ and $\mathbf{E} \parallel [110]$ yield nearly identical spectra. This is consistent with the selection rules for the hh- and lh-excitonic transitions for a GaAs(001) thin film under a biaxial stress in which the stress tensor, σ, has equal orthogonal components, $\sigma_{\parallel} = \sigma_{\perp}$. Under a biaxial tensile stress the preferential direction for the quantization of the hole angular momentum (m_j) is along <001>, emission along this direction is unpolarized in the (001) surface plane as observed, and the lh exciton (identified as peak P_1) is the lowest energy transition [3, 26].

The hh and lh excitonic peak positions from the fits of Figure 18 are shown in Figure 19 for the various mesa sizes. The stress-induced lh-to-hh energy splitting reduces from 13.4 meV for the largest mesa (1 mm) to 3.4 meV for the smallest mesa (10 μm). For a biaxial stress in GaAs, the hh-to-lh energy splitting increases at a rate of ~ 6.2 meV/kbar from eq. (3). The bottom of Figure 19 shows that the magnitude of the stress reduces from ~ 2.2 kbar for the 1 mm mesa to 0.5 kbar for the

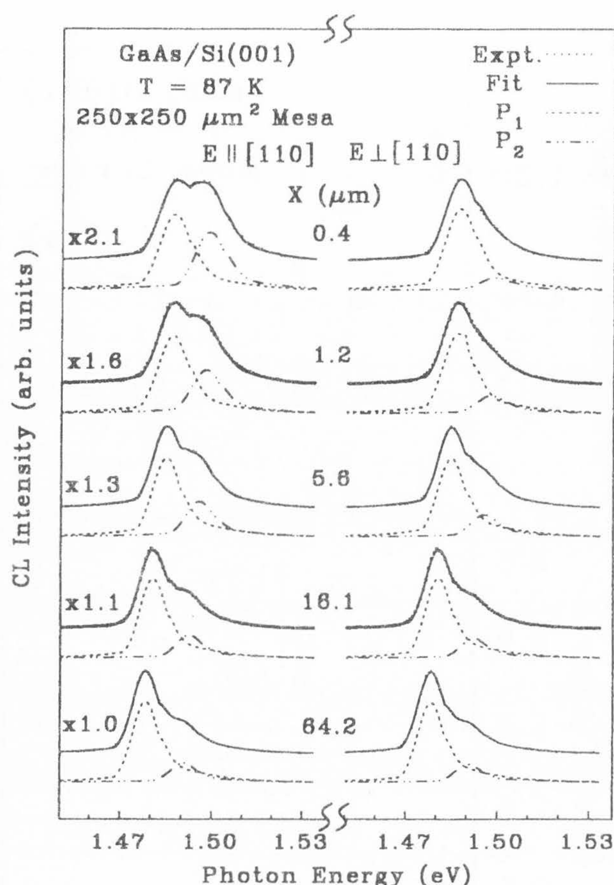

Figure 20. Local polarized CL spectra as a function of the distance from the edge of the 250 μm mesa for the polarizer detection orientations of $\mathbf{E}\perp[110]$ and $\mathbf{E}\parallel[110]$. The decomposition of the luminescence lineshape into two components (labeled as P_1 and P_2) resulting from the strain-induced splitting of the top valence bands is shown. The overall fit to the data is indicated by a solid line running through the data. The factors used to scale spectra for $\mathbf{E}\parallel[110]$ detection relative to the spectra for $\mathbf{E}\perp[110]$ detection are shown.

---

10 μm mesa. This result is consistent with the PL measurements of Lingunis *et al.* [19], which showed a similar stress reduction for a 10 μm mesa that was 1 μm thick.

Further investigation shows that stress on 10 μm mesa evaluated from the peak positions does not vary significantly with location, though stress on 25 μm mesa has a slight variation throughout the mesa. It is widely accepted that in the vicinity of edge, the mismatched lattice is free to relax [27, 35, 41], resulting in a stress relief in direction perpendicular to the edge. Analytical and numerical models have been proposed in studying the stress relief near edges of heteroepitaxial layer [20, 33, 37]. The existence of biaxial stress has been established at the centers of all mesas, and the presence of the mesa edge will affect the stress in the vicinity of the mesa edge. Previously, we have shown that near microcracks the GaAs film is subject to uniaxial stress which transforms to biaxial stress for regions greater than ~ 15 μm away from the cracks [27]. A similar effect should also occur near the mesa edges, where the stress tensor is also free to relax along the direction normal to the edge, resulting in an approximate uniaxial stress. We can describe this stress reduction by introducing a parameter L_D, the decay length of stress relief and the pattern half-width W. The stress component $\sigma_\perp$, as a function of the distance from the center, can be expressed using the following bi-metal thermostat model [37]:

$$\sigma_\perp(x) = \sigma_m \left\{ 1 - \frac{\cosh(x/L_D)}{\cosh(W/L_D)} \right\} + \sigma_0 \tag{4}$$

where x is the distance from the center and σ_m is the maximum stress reduction at the edge, and σ_0 is the residual stress remaining at the edge. When the size of pattern is much larger than L_D, the effect of the edge on stress relief is very small and the biaxial stress at the center region is independent of the size. However, if the size of mesa is comparable to L_D, the edge becomes an important source of stress relief, the stress should strongly depend on the size of mesa.

The scanning capability of the SEM allows us to investigate μm-scale spatial variations. To further investigate the stress distribution on the mesa and confirm the model of eq. (4), spectra were taken for mesa sizes ranging from 10 to 1000 μm, as a function of the distance from the edge of mesa, by fixing the electron beam at positions along the path parallel to $[1\bar{1}0]$ from the edge to the center. The experimental results indicate that as the electron beam scans from the center towards the edge, the position of the exciton peaks shifts to higher energies and the splitting of P_1 and P_2 exciton peaks reduces. Figure 20 shows a stack plot of local polarized CL spectra taken as a function of distance from the [110]-oriented edge of the 250 μm square mesa. The resulting positions of peaks P_1 and P_2 obtained from the fits for the 250 μm mesa are plotted in Figure 21. A distinct increase in the polarization anisotropy for the polarizer orientations used to detect emissions with $\mathbf{E}\perp[110]$ and $\mathbf{E}\parallel[110]$ is observed as the beam is positioned close to the mesa edge. For a pure [110] uniaxial tensile stress along [110], the preferential direction for quantization of the hole angular momentum, m_j, is along [110], and the lowest energy transition (P_1) has primarily a hh character [3, 26]. Thus, regions of pure biaxial

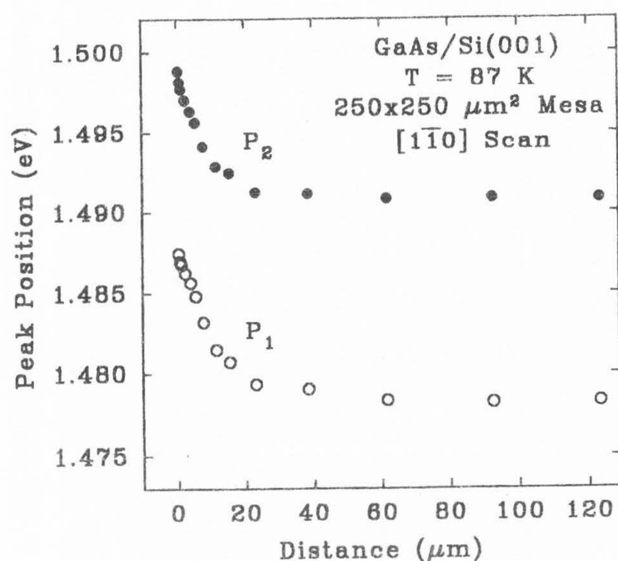

Figure 21. Energy positions of the strain split peaks P_1 and P_2 as a function of the distance from the [110]-oriented edge of the 250 μm mesa.

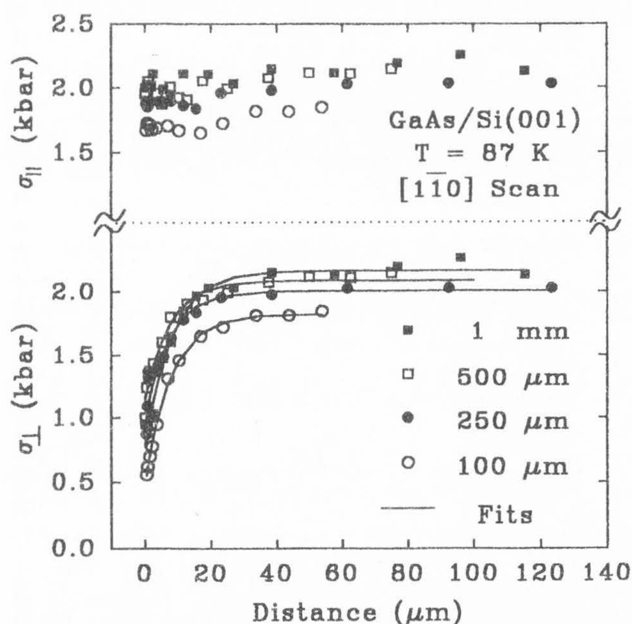

Figure 22. The calculated stress components $\sigma_{\parallel}$ and $\sigma_{\perp}$, using eq. (3) and the condition $\sigma_z = \tau = 0$, as a function of the distance from the edge for the mesa sizes indicated. The fits to the data using the model of eq. (4) are indicated by the solid lines in the figure.

and pure uniaxial stress must have a reversed energy order for the hh and lh excitonic transitions (see Fig. 17). The hh-excitonic transition for pure uniaxial tensile

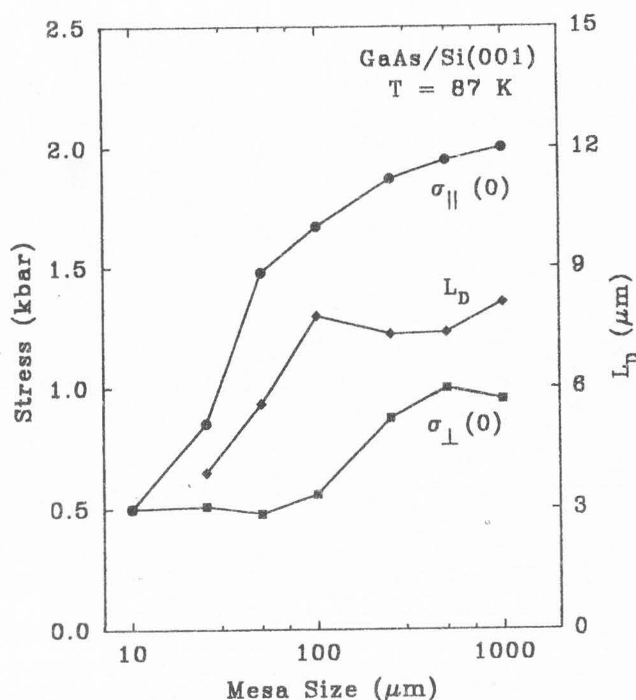

Figure 23. The decay length L_D, the parallel stress $\sigma_{\parallel}$, and the residual stress $\sigma_{\perp}$ as a function of the mesa size using solutions to the bi-metal decay model and the orbital-strain Hamiltonian, as described by eqs. (4) and (3), respectively. The values for $\sigma_{\parallel}$ and $\sigma_{\perp}$ at the mesa edges (x = 0) are indicated by filled circles and squares, respectively, assuming $\sigma_z = \tau = 0$.

stress results in emission which is linearly polarized perpendicular to the mesa edge [3, 26, 27]. In Figure 20 for x = 0.4 μm, the hh-to-lh peak intensity ratio changes from 6.4 to 1.3 as the polarizer is rotated from the $\mathbf{E}\perp[110]$ to $\mathbf{E}\parallel[110]$ detection orientations. This confirms the strong uniaxial character of the stress at the mesa edge [27].

Determination of local stress tensor

Quantitatively, we can deduce, from the positions of the excitonic transitions, the stress components along two orthogonal <110> directions, $\sigma_{\perp}$ and $\sigma_{\parallel}$, by utilizing eq. (3) without including shear and peeling stress terms (i.e., $\sigma_z = \tau = 0$). The energy of the excitonic transition for zero applied stress, E(0), was determined by examining the luminescence from MOCVD grown GaAs on GaAs(001) grown under the same conditions. A result of E(0) = 1.506 eV was found at 87K. Figure 22 shows the stress components $\sigma_{\parallel}$ and $\sigma_{\perp}$ as a function of distance for different mesa sizes derived from the results of Figure 21 and data for the other mesas not shown here. The results of Figure 22 show that $\sigma_{\parallel}$ does not vary significantly with distance, although the stress increases as the mesa size increases. Because of the re-

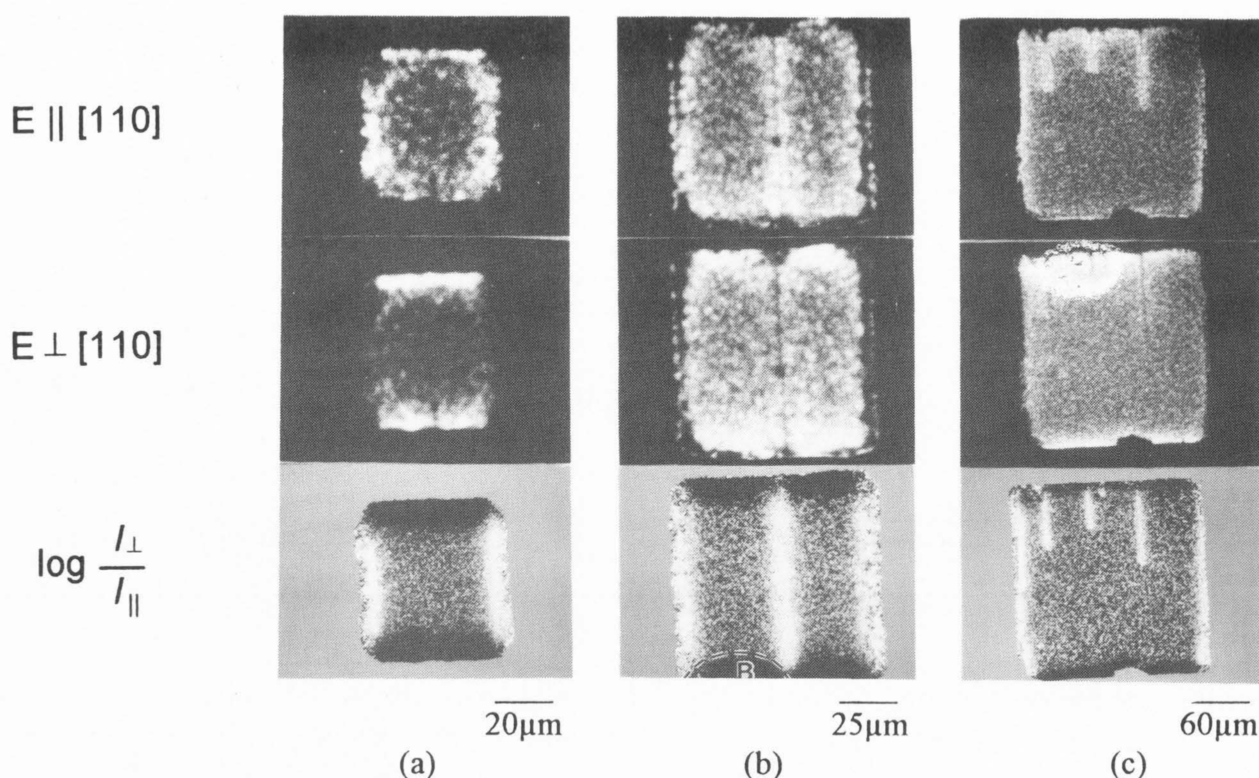

Figure 24. Linearly polarized CL images for mesa sizes of 50 (**a**), 100 (**b**) and 250 μm (**c**). For each mesa, three images showing the polarization detection conditions of $\mathbf{E} \perp [110]$, $\mathbf{E} \parallel [110]$ and $\log(I_\perp/I_\parallel)$ are indicated. The shape of a biaxial stress boundary contour, for example, can be identified as a dashed line near the region labeled B in (**b**).

duction of $\sigma_\perp$, the character of stress changes from biaxial at the center to nearly uniaxial at the edge, as also confirmed by the polarization anisotropy of hh excitonic transition near the edges of all mesas. For $x \gtrsim 15$ μm the lh and hh transitions have the same intensities for the two polarization directions for all mesas studied here, which is consistent with the selection rules for biaxial stress as previously discussed. It can be seen that the stress reduction behavior for different sizes are very similar. The fitting of $\sigma_\perp(x)$ with eq. (4) is shown with lines through the data of Figure 22.

The results of the fits showing L_D versus the mesa size are shown in Figure 23. The decay length L_D is seen to increase from 3.9 to 7.8 μm as the mesa size increases from 25 to 100 μm after which no significant change in L_D is found. It is evident, when considering eq. (4), that L_D decreases for mesas less than 100 μm because the size of the mesa becomes comparable to L_D, and all four edges of the square will interact in relieving the stress. For the 10 μm mesa, no detectable decay in the stress was observed as the beam was positioned from the mesa edge, indicating a completely homogenous stress as reported above. The residual tensile stress remaining at the $x = 0$ edge, $\sigma_\perp(0)$, is seen to fluctuate between 0.5 and 1 kbar in Figure 22. An increase in $\sigma_\perp(0)$ is seen for mesa sizes greater than 100 μm. The experimentally determined values of $\sigma_\perp(0)$ and $\sigma_\parallel(0)$ are shown in Figure 23 as a function of the mesa sizes. The relaxation of $\sigma_\perp$ at the mesa edge has been examined with finite element elastic calculations; a maximum value of ~ 0.2 kbar has been calculated [20, 21]. There are additional types of edge-related stresses, as indicated in eq. (3) by the presence of peeling (σ_z) and shear (τ) terms. These terms can generally be comparable in magnitude to $\sigma_\parallel$ and $\sigma_\perp$ for thermally mismatched thin films, as indicated in the calculations of Suhir [37] who showed that a tensile peeling stress and non-zero shear stress can exist near the edge a thin film. Also, with any luminescence technique involving electron-hole excitation, the magnitude of the stress near the edges is uncertain due to the ~ 0.5 μm minority carrier diffusion length. The approximately exponentially decay (see eq. (4) for small x) of stress near the edge results in an exponential increase in the bandgap (from eq. (3)) as the

edge is approached. This gradient in the bandgap could induce excess electrons and holes to drift away from the edge or corners to a region of lower bandgap, resulting in an effective increase in measured $\sigma_{\perp}$ values. However, our lack of knowledge of the bandbending in the vicinity of the mesa edges and surface precludes any quantitative assessment of this effect.

Linearly Polarized CL imaging of GaAs/Si

In order to assess the homogeneity of the optical quality of the entire mesa region, it is necessary to employ the CL imaging capability. The optical quality can vary from point to point on the GaAs mesa as a result of dislocations and stacking faults resulting from the large lattice mismatch between Si and GaAs. Imperfections in the etching of the SiO_2 mask before GaAs growth and its chemical removal after growth can lead to deviations from a perfect square mesa pattern, and subsequently lead to inhomogeneities in thermal stress. The microcracks resulting from the thermal stress will occur when the mesa size exceeds a critical value, and CL imaging can be used to determine this. A useful non-destructive approach to obtain immediate feedback on the quality of device structure and its degree of homogeneity is to perform CL imaging. In particular, polarized CL imaging can enable the immediate identification of regions which deviate from an ideal biaxial stress. Figure 24 shows monochromatic LPCL images of the 50, 100, and 250 μm mesas. Photon energies of 1.494 eV (50 μm mesa) and 1.487 eV (100 and 250 μm mesas) were detected in the monochromatic LPCL imaging. The photon energies were chosen so as to correspond to the peak of the hh-excitonic transition that occurs near the edges of the mesas. The images were taken with the polarizer rotated to detect emission of light with $E \perp [110]$ and $E \parallel [110]$ detection orientations, as indicated in the figure. When the polarizer is oriented so as to detect emission with $E \perp [110]$, the regions near the square mesa edges which are parallel and perpendicular to [110] become bright and dark, respectively. This is a result of the linearly polarized property of excitonic emission associated with the hh wavefunction, as discussed above. Also, in order to emphasize the regions which show a polarization dependence, the ratio of the images is displayed. The pixels in the ratio images at a (x,y) position are represented as:

$$\log[I_{\perp}(x,y)/I_{\parallel}(x,y)]$$

where $I_{\perp}(x,y)$ and $I_{\parallel}(x,y)$ are the pixel intensities under $E \perp [110]$ and $E \parallel [110]$ detection orientations, normalized to a 256 level grey scale. Regions of uniform bright and dark contrast indicate deviations from biaxial stress and occur near regions of uniaxial stress. For

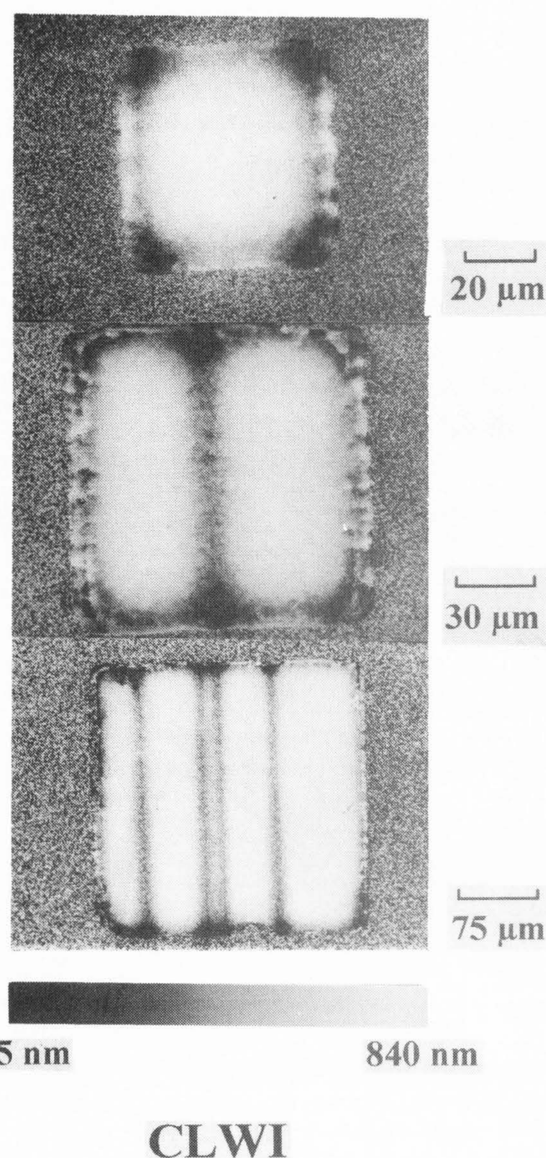

Figure 25. CLWI images of the same 50, 100, and 250 μm mesas shown in Figure 24. The wavelength scale indicates the wavelength of peak intensity for the excitonic luminescence. The long- and short-wavelength emissions correlate spatially with regions of biaxial and uniaxial stress, respectively. The regions of shortest wavelength (dark) correspond to complete stress relief which is caused by intersecting microcracks and edges. Thermal cycling of the sample or, possibly, exposure to the electron beam has caused the partial microcracks seen in Figure 24c to propagate across the entire mesa.

---

mesa sizes greater than or equal to 100 μm, microcracks were found to run parallel to [110], as can be seen in Figures 24b and 24c. The polarization dependence of the luminescence near the microcracks is similar to that

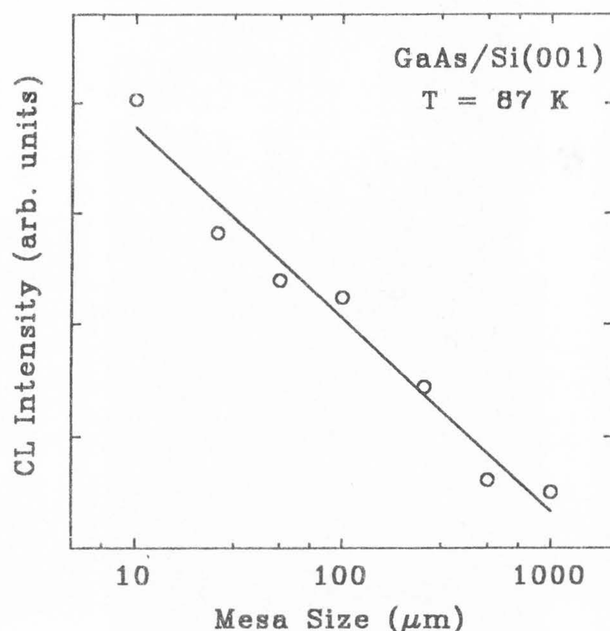

Figure 26. The integrated cathodoluminescence intensity as a function of the mesa size. The solid line indicates a linear fit and shows a logarithmic dependence of the CL intensity on the mesa size.

near the mesa edges, and the microcracks were previously found to exhibit a nearly uniaxial stress dependence [27]. The shape of the biaxial stress boundary contours can be seen near regions of constant intensity away from the microcracks and edges in the ratio images (see, e.g., dashed line in Fig. 24b). Figure 24c shows results from a non-ideal 250 μm mesa containing microcracks and defects near the meas edges. Again, the bright and dark regions pinpoint regions of stress relief. The microcracks do not necessarily propagate through the entire mesa, as seen in Figure 24c, but thermal cycling of the sample can induce microcrack propagation (as seen in a subsequent CL image discussed below). Thus, polarized CL image can sensitively identify small deviations from pure biaxial stress resulting from defects.

CL wavelength imaging of GaAs/Si

In order to further assess spatial variations in the stress, we have examined the cathodoluminescence wavelength images (CLWI) of the GaAs/Si sample. In CLWI, the wavelength as a function of the spatial (x,y) position, $\lambda_m(x,y)$, at which there is a peak in the intensity of a local luminescence spectrum, is determined, and a modified-color or grey-scale image directly mapping these wavelengths is generated [10]. In this study, the scanning area was discretized into 640 x 480 pixels. In order to determine $\lambda_m(x,y)$, a spectrum consisting of 31 wavelength points (obtained from 31 discrete monochromatic CL images), varying from 825 to 840 nm, was obtained at each pixel position. CLWI images of the same mesas depicted in Figure 24 are shown in Figure 25. The speckled regions delineate the non-luminescent Si substrate. The grey-scale bar showing the wavelength mapping of $\lambda_m(x,y)$ is shown, and the dark regions represent peak positions shifted towards shorter wavelengths. The regions of longer wavelength (brighter regions) are seen to occur at least ~ 10-20 μm from the edges, indicating regions of uniform biaxial tensile stress that accompany bandgap lowering. Near the edges and microcracks, $\lambda_m(x,y)$, generally shifts towards shorter wavelengths, but some variation is seen to due to inhomogeneities in edge quality. The result is similar and complementary to the LPCL images of Figure 24 and allows the determination of regions exhibiting biaxial and uniaxial stress and regions of complete stress relief (such as at the intersection of microcracks and edges which are dark in Fig. 24). Figures 24c and 25c are of the same 250 μm mesa taken at different times. The thermal cycling of the sample and, perhaps, repeated exposure to the electron beam have induced the partial cracks (Fig. 24c) to elongate across the entire mesa (Fig. 25c).

Influence of GaAs mesa size on optical and structural quality

The selective growth of thin films on reduced areas is known to enhance the optical and structural quality of the film when the epilayer and substrate are lattice mismatched [12, 19]. Yamaguchi *et al.* [42] recently showed a reduction in the dislocation density, using the etch-pit method, for MOCVD selectively grown GaAs on Si. It was argued that the reduction in thermal stress present for the smaller pattern sizes would lead to a reduction in the stress-induced dislocation density, and a linear correlation between stress and dislocation density was established by these authors. The integrated CL intensity is shown versus the mesa size in Figure 26. The CL intensity is found to decrease nearly logarithmically with the mesa size, thus indicating an increase in the structural quality of the GaAs films for smaller mesa sizes. These results do, therefore, confirm that stress induced dislocations, whether thermal or lattice-mismatch in nature, can be reduced through selective growth on reduced areas.

Conclusion

We have utilized novel SEM-based optical imaging techniques to study the optical properties of *nipi*-doped $In_{0.2}Ga_{0.8}As/GaAs$ MQWs and mesas of GaAs/Si. The former system exhibits strain-induced defects mainly as a result of lattice mismatch, while the latter, in addition to lattice mismatch, suffers from a stress-induced by a

difference in thermal expansion coefficient.

The modulation of MQW exciton absorption has been demonstrated with use of a high-energy electron beam to study the carrier recombination dynamics. The spatially separated electron-hole plasma created in the *nipi*-doped MQWs is used as a probe in EBIA to study the influence of strain-induced defects on the ambipolar diffusive transport of carriers. The modulation in absorption coefficient is illustrated with two types of *nipi* MQW structures which involve (i) filling of QW states and subsequent screening of the hh1-e1 excitonic Coulombic interaction and (ii) modifying the electric field experienced by the QWs and thereby inducing a change in the quantum confined Stark effect of the hh1-e1 excitonic absorption energy. An anisotropy in the ambipolar diffusive transport is observed in EBIA imaging of the QCSE sample which stems from the anisotropy in nucleation and propagation of α-type and β-type dislocation cores. Electron beam energy-dependent CL imaging and the corresponding histogram analysis indicates that non-radiative recombination centers in the MQW giving rise to DLDs are group at various distances from the GaAs substrate. The position and orientation of steps in EBIA is directly correlated with DLDs observed in CL images indicating that potential fluctuations induced by misfit dislocations and a Cottrell atmosphere of defects will impede carrier transport. For a *nipi*-doped MQW sample which exhibits little DLD contrast, the corresponding EBIA image is found to by cylindrically symmetric without any noticeable steps. A direct μm-scale imaging of the effects of structural defects on transport is demonstrated with EBIA.

We have examined the variation of stress tensor in selective area MOCVD grown GaAs on Si substrate by using a LPCL technique. Patterns with smaller dimension show better optical quality, indicating a reduction in the thermal stress induced dislocation density. The biaxial stress is found to decrease for small mesa sizes, and a stress reduction near the edges is modeled well with a bi-metal thin film model. A residual stress (0.5-1.0 kbar) exists on the corner. The CL results show that (i) the decay length of stress relief near a pattern edge increases with increasing mesa size, (ii) the maximum biaxial stress and residual stress near the mesa edges increase with increasing pattern size, and (iii) the luminescence efficiency of the film decreases with increasing pattern size. The stress components $\sigma_{\parallel}$ and $\sigma_{\perp}$ can be determined as a function of position from the LPCL strain-split peak positions and solutions to the orbital-strain Hamiltonian. The selective-area growth method improves the quality of thermally mismatch epilayer materials and helps to reduce the thermal stress on the heteroepitaxial layer. Polarized CL imaging is observed to be sensitive to local deviations from biaxial stress and can be used to map the boundaries of stress contours near mesa edges and defects. CLWI reveals additional information on stress-relief by allowing a direct spatial imaging of bandgap variations. The versatility of state-of-the-art SEM systems combined with the ease of interface and control with inexpensive PC-based microcomputers with powerful image processing and data manipulation capabilities facilitates the development of new techniques for studying the interrelationship between microstructure, optical, and transport properties.

Acknowledgement

This work was supported in part by grants from the USC James H. Zumberge Faculty Research and Innovation Fund, the Charles Lee Powell Foundation, the National Science Foundation (RIA-ECS), and the U.S. Army Research Office. We would like to thank Dr. N.H. Karam of Spire Corporation for the GaAs/Si samples examined in this study.

References

[1] Abrahams MS, Blanc J, Buiocchi CJ (1972) Like-sign asymmetric dislocations in zinc-blende structure. Appl Phys Lett **21**, 185-186.

[2] Ball CAB, van der Merwe JH (1983) The growth of dislocation-free layers. In: Dislocations in Solids. Nabarro FRN (ed.). North-Holland, Amsterdam. Chapter 27.

[3] Chandrasekhar M, Pollak FH (1977) Effects of uniaxial stress on the electroreflectance spectrum of Ge and GaAs. Phys Rev **B15**, 2127-2144.

[4] Döhler GH (1986) Doping Superlattices ("nipi Crystals"). IEEE J Quant Electron **22**, 1682-1695.

[5] Dutta M, Shen H, Vernon SM, Dixon TM (1990) Photoreflectance study of gallium arsenide grown on Si. Appl Phys Lett **57**, 1775-1777.

[6] Everhart TE, Hoff PH (1971) Determination of kilovolt electron energy dissipation vs. penetration distance in solid materials. J Appl Phys **42**, 5837-5846.

[7] Fitzgerald EA, Watson GP, Proano RE, Ast DG, Kirchner PD, Pettit GD, Woodall JM (1989) Nucleation mechanisms and the elimination of misfit dislocations at mismatched interfaces by reduction in growth area. J Appl Phys **65**, 2220-2237.

[8] Fox BA, Jesser WA (1990) The effect of frictional stress on the calculation of critical thickness in epitaxy. J Appl Phys **68**, 2801-2808.

[9] George T, Weber ER, Nozaki S, Yamada T, Konagai M, Takahashi K (1991) Critical thickness anisotropy in highly carbon-doped p-type (100)GaAs layers grown by metalorganic molecular beam epitaxy. Appl Phys Lett **59**, 60-62.

[10] Grundmann M, Christen J, Bimberg D, Hashimoto A, Fukunaga T, Watanabe N (1991) Direct imaging of Si incorporation in GaAs masklessly grown on patterned Si substrates. Appl Phys Lett **58**, 2090-2092.

[11] Jesser WA, Fox BA (1990) On the generation of misfit dislocations. J Electron Mater **19**, 1289-1297.

[12] Karam NH, Haven V, Vernon SM, El-Masry N, Lingunis EH, Haegel NM (1991) Selective area epitaxy of GaAs on Si using atomic layer epitaxy by LP-MOVPE. J Cryst Growth **107**, 129-135.

[13] Kavanagh KL, Capano MA, Hobbs LW, Barbour JC, Maree PMJ, Schaff W, Mayer JW, Petit D, Woodall JM, Stroscio JA, Feenstra RM (1988) Asymmetries in dislocation densities, surface morphology, and strain of GaInAs/GaAs heterolayers. J Appl Phys **64**, 4843-4852.

[14] Kroemer H (1987) Polar on nonpolar epitaxy. J Cryst Growth **81**, 193-204.

[15] Larsson A, Maserjian J (1991) Optically induced absorption modulation in a periodically δ-doped InGaAs/GaAs multiple quantum well structure. Appl Phys Lett **58**, 1946-1948.

[16] Larsson A, Maserjian J (1991) Optically induced excitonic electroabsorption in a periodically δ-doped InGaAs/GaAs multiple quantum well structure. Appl Phys Lett **59**, 1946-1948.

[17] Larsson A, Maserjian J (1991) Optically addressed asymmetric Fabry-Perot modulator. Appl Phys Lett **59**, 3099-3101.

[18] Larsson AG, Jonsson B, Sjölund O, Cody J, Andersson TG, Wang S, Södervall U, Rich DH, Maserjian J (1993) Carrier lifetimes in periodically δ-doped MQW structures. SPIE Proc **1985**, 478-489.

[19] Lingunis EH, Haegel NM, Karam NH (1990) Photoluminescence studies of stress relief in selectively grown GaAs on Si by metalorganic chemical vapor deposition. Solid State Commun **76**, 303-306.

[20] Lingunis EH, Haegel NM, Karam NH (1991) Thermal stresses in square-patterned GaAs/Si: A finite element study. Appl Phys Lett **59**, 3428-3430.

[21] Lingunis EH, Haegel NM, Karam NH (1993) Cathodoluminescence studies and finite element analysis of thermal stresses in GaAs/Si stripes. J Appl Phys **74**, 2779-2785.

[22] Liu TY, Petroff PM, Kroemer H (1988) Luminescence of GaAs/(Al,Ga)As superlattices grown on Si substrates containing a high density of threading dislocations: Strong effect of the superlattice period. J Appl Phys **64**, 6810-6814.

[23] Maserjian J, Andersson PO, Hancock BR, Iannelli JM, Eng ST, Grunthaner FJ, Law KK, Holtz PO, Simes RJ, Coldren LA, Gossard AC, Merz JL (1989) Optically addressed spatial light modulators by MBE-grown nipi MQW structures. Appl Optics **28**, 4801-4807.

[24] Matthews JW, Blakeslee AE (1974) Defects in epitaxial multilayers I. Misfit dislocations. J Cryst Growth **27**, 118-125.

[25] Miller DAB, Chemla DS, Damen TC, Gossard AC, Wiegmann W, Wood TH, Burrus CA (1985) Electric field dependence of optical absorption near the band gap of quantum well structures. Phys Rev B**32**, 1043-1060.

[26] Pollak FH, Cardona M (1968) Piezo-electroreflectance in Ge, GaAs, and Si. Phys Rev **172**, 816-837.

[27] Rich DH, Ksendzov A, Terhune RW, Grunthaner FJ, Wilson BA, Shen H, Dutta M, Vernon SM, Dixon TM (1991) Polarized-cathodoluminescence study of uniaxial and biaxial stress in GaAs/Si. Phys Rev B**43** 6836-6839.

[28] Rich DH, George T, Pike WT, Maserjian J, Grunthaner FJ, Larsson A (1992) Cathodoluminescence and transmission electron microscopy study of dark line defects in thick $In_{0.2}Ga_{0.8}As$/GaAs multiple quantum wells. J Appl Phys **72**, 5834-5839.

[29] Rich DH, Lin HT, Larsson A (1995) Influence of defects on electron-hole plasma recombination and transport in a nipi-doped InGaAs/GaAs multiple quantum well structure. J Appl Phys **77**, 6557-6568.

[30] Rich DH, Rammohan K, Tang Y, Lin HT, Maserjian J, Grunthaner FJ, Larsson A, Borenstain SI (1993) Absorption modulation induced by electron beam excitation of strained $In_{0.2}Ga_{0.8}As$/GaAs multiple quantum wells. J Vac Sci Technol B**11**, 1717-1722.

[31] Rich DH, Rammohan K, Tang Y, Lin HT, Maserjian J, Grunthaner FJ, Larsson A, Borenstain SI (1994) Ambipolar diffusion anisotropy induced by defects in nipi-doped $In_{0.2}Ga_{0.8}As$/GaAs multiple quantum wells. Appl Phys Lett **64**, 730-732.

[32] Rosenberg JJ, Benlamri M, Kirchner PD, Woodall JM, Pettit GD (1985) An $In_{0.15}Ga_{0.85}As$/GaAs pseudomorphic single quantum well HEMT. IEEE Electron Devices Lett **EDL-6**, 491-493.

[33] Sakai S, Kawaski K, Wada N (1990) Stress distribution analysis in structured GaAs layers fabricated on Si substrates. Jpn J Appl Phys **29**, L853-L855.

[34] Schaff WJ (1991) Device applications of strained-layer epitaxy. In: Semiconductors and Semimetals, Vol. 33. Willardson RK, Beer AC (eds.). Academic Press, New York. pp. 73-138.

[35] Shen H, Dutta M, Eckart DW, Jones KA, Vernon SM, Dixon TM (1990) Biaxial and uniaxial stress in gallium arsenide on silicon: A linear polarized photoluminescence study. J Appl Phys **68**, 369-371.

[36] Streibl N, Brenner KH, Huang A, Jahns J, Jewell J, Lohmann AW, Miller DAB, Murdocca M, Prise ME, Sizer T (1989) Digital optics. Proc IEEE, **77**,

1954-1969.

[37] Suhir E (1989) Interfacial stresses in bimetal thermostats. ASME J Appl Mech **56**, 595-600.

[38] van der Ziel JP, Chand N, Weiner JS (1989) Elimination of thermally induced biaxial stress in GaAs on Si layers by post-growth patterning. J Appl Phys **66** 1195-1198.

[39] Wang J, Steeds JW, Woolf DA (1992) The study of misfit dislocations in $In_xGa_{1-x}As/GaAs$ strained quantum well structures. Phil Mag A**65**, 829-839.

[40] Wilson BA, Bonner CE, Miller RC, Sputz SK, Harris TD, Lamont MG, Dupis RD, Vernon SM, Haven VE, Lum RM, Klingert JK (1988) Photoluminescence studies of heteroepitaxial GaAs on Si. J Electron Mater **17**, 115-119.

[41] Yacobi BG, Jagannath C, Zemon S (1988) Stress variations and relief in patterned GaAs grown on mismatched substrates. Appl Phys Lett **52**, 555-557.

[42] Yamaguchi M, Tachikawa M, Sugo M, Kondo S, Itoh Y (1990) Analysis for dislocation density reduction in selective area grown GaAs films on Si substrates. Appl Phys Lett **56**, 27-29.

[43] Yonenaga I, Sumino K (1989) Impurity effects on the generation, velocity, and immobilization of dislocations in GaAs. J Appl Phys **65**, 85-92.

[44] Zou J, Cockayne DJH, Usher BF (1993) Misfit dislocations and critical thickness in InGaAs/GaAs heterostructure systems. J Appl Phys **73**, 619-626.